Graphical Abstract

Deep-reactive-ion-etching in X-ray grating fabrication: a review

Zhitian Shi, Konstantins Jefimovs, Joan Vila-Comamala, Alexandre Pereira, Daniel Josell, Marco Stampanoni, Lucia Romano

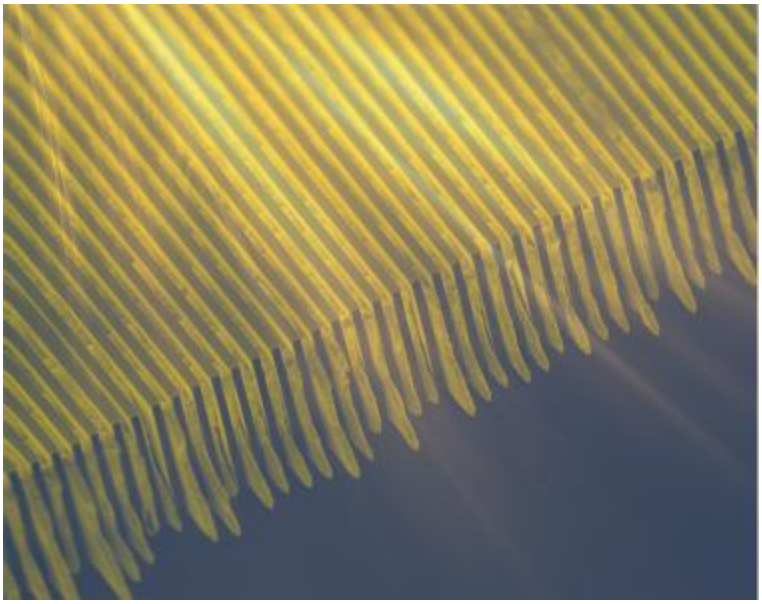

Highlights

Deep-reactive-ion-etching in X-ray grating fabrication: a review

Zhitian Shi, Konstantins Jefimovs, Joan Vila-Comamala, Daniel Josell, Marco Stampanoni, Lucia Romano

- This paper gives an overview of recent progress in the silicon-based microfabrication of X-ray gratings
- A detailed fabrication process from the grating design to the tuning protocol of plasma etching of silicon is provided
- The process flow can be adapted for the fabrication of different kinds of high-aspect-ratio microstructures

Deep-reactive-ion-etching in X-ray grating fabrication: a review

Zhitian Shi[a,b,c,d], Konstantins Jefimovs[a], Joan Vila-Comamala[a], Alexandre Pereira[a,b], Daniel Josell[e], Marco Stampanoni[a,b], Lucia Romano[a,b]

[a]*Paul Scherrer Institut, 5232 Villigen PSI, Switzerland*
[b]*Institute for Biomedical Engineering, ETH Zurich, 8092 Zurich, Switzerland*
[c]*Electrical Engineering Division, Department of Engineering, University of Cambridge, U.K.*
[d]*Now at Center for Functional Nanomaterials, Brookhaven National Laboratory, U.S.*
[e]*Materials Science and Engineering Division, National Institute of Standards and Technology, Gaithersburg, Maryland 20899, USA*

Abstract

The development of grating fabrication shares its journey with the development of X-ray phase contrast imaging. Indeed, the fabrication of gratings with features of sufficiently high aspect ratio is one of the bottlenecks preventing the widespread application of phase contrast imaging in X-ray diagnostics, material science and security. The silicon platform that underlies modern manufacture of integrated circuits, with its well-established technologies for lithography, etching and metal deposition, has the potential to provide high yields and volumes for industrial fabrication of both phase and absorption gratings used in a grating-based X-ray imaging systems. This review article introduces recent developments in the fabrication of high aspect ratio X-ray gratings using ubiquitous clean-room manufacturing tools, focusing on deep reactive ion etching processes. It summarizes the most challenging issues for fabricating features with aspect ratios reaching 70:1, proposing approaches to overcome processing problems and improve product quality.

Keywords*: deep reactive ion etching, high aspect ratio structures, gratings, X-ray imaging, neutron imaging, lithography, microfabrication, metrology*

Email address: zshi2@bnl.gov (Zhitian Shi)

Contents

1. Introduction

1.1 X-ray Grating Interferometry

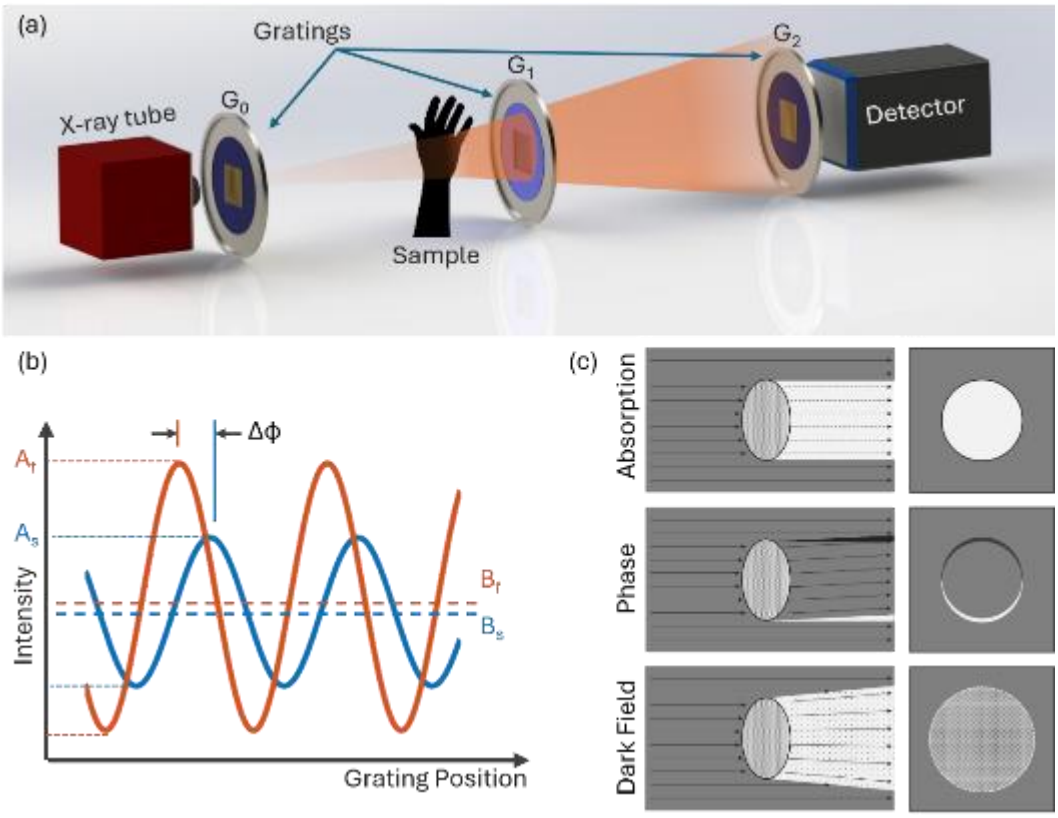

Figure 1: Schematics of (a) a classic Talbot-Lau Interferometry system with three gratings G0, G1, G2, (b) the phase stepping curves retrieved at one of the pixels on the detector, with (blue, label *s*) and without (red, label *f*) the test sample (see the text for details). The attenuation signal is calculated from B_f/B_s, the phase shift is $\Delta\phi$, and the dark field signal is calculated from A_sB_f/A_fB_s, and (c) schematics for the origin of the three different types of X-ray signals from the sample. Figure adapted with permission from ref. [1].

Since Röntgen's discovery that X-rays can reveal bone structures, X-ray imaging has become an essential tool in medical diagnostics, failure analysis, and materials science. However, the commonly used X-ray absorption contrast mechanism is ineffective for objects composed of weakly absorbing matter (e.g., low Z-elements) such as biological soft tissues or carbon reinforced polymers that offer small absolute variation in optical properties. Grating-based X-ray interferometric (XGI) imaging, with early experiments performed on synchrotrons [2] and later experiments with laboratory sources exploiting phase [3] and dark field [4] contrasts, offers a superior option for such materials. This technique has high potential for medical diagnostics [5-8] as well as being a powerful method for the non-destructive imaging of interior structures for applications in materials science [9] and security [10]. However,

because the angular sensitivity of the interferometer increases as the grating pitch decreases, small grating pitch are needed for materials exhibiting small refraction angle [11]. Gratings with metal lamellas at micrometer- or even sub-micrometer-scale pitch are typically required. At the same time, medical diagnostics applications require hard X-rays (> 30 keV), for which the height of the metal features must be in a range of tens or even hundreds of micrometers, depending on the X-ray energy used and the metal material. This requires very high aspect ratio grating structures, e.g., lamella's height to width ratio (AR) higher than 50:1, and highly absorbing metals such as gold. Further, because the field of view of the imaging technique depends directly on the physical size of the grating, patterning must be accomplished with high precision over large areas (e.g., larger than 50 cm^2). The assessment of grating quality in the high aspect ratio regime remains challenging since the metrology to investigate the presence of defects and their nature (e.g., the geometrical fidelity of the grating, aspect ratio, line width, uniformity, bar tilt, verticality, etc.) is limited to local characterization, while the functional performance metrics (e.g., visibility and diffraction efficiency) are related to large area non-local effects [12-14]. As the gratings are key to detecting subtle variation in the interferometric patterns underlying imaging, local as well as overall uniformity of the grating features is critical for performance. Grating features such as pitch size, duty cycle (DC, i.e., the ratio of transmitting line width to grating pitch) and their uniformity over the patterned area [15], are usually characterized by scanning electron microscopy (SEM), with all the artefacts and criticalities of a destructive procedure to realize a cross section and only when the material allows it. The ultimate performance of a grating in XGI depends on the specific system configuration. While several non-destructive methods exist to characterize the grating quality for low aspect ratio structures, including optical profilometry, X-ray diffraction efficiency mapping [16-18], large-area rocking curves measurements [19] and support of optical simulations [14, 20] are needed for high aspect ratio gratings. Visibility (see below) is commonly accepted as a figure of merit of the interferometric set-up [21], but it depends on features of the system, including the X-ray spectrum and detector, in addition to the actual grating quality. In XGI, visibility is a measure of fringe contrast and is commonly used as a performance metric for evaluating grating quality. It is defined as $V = (I_{max} - I_{min}) / (I_{max} + I_{min})$, where I_{max} and I_{min} are the maximum and minimum intensities of the interference fringes, respectively. As a general rule, then, the visibility value cannot be absolutely ascribed to grating quality. That said, visibility maps across the field of view can support the evaluation of grating uniformity as well as relative comparisons. The efficiency of interferometric systems is characterized by the sensitivity, defined as the product of visibility and the square root of the transmitted photon counts. Sensitivity is directly proportional to the signal to noise ratio, making it a crucial parameter for assessing the overall performance of imaging systems[22].

Grating-based X-ray imaging requires only moderate spatial coherence, making it a promising technique for use without synchrotron sources [3]. However, for clinical

applicability, the technology must be compatible with conventional laboratory sources such as X-ray tubes. While compact or so-called 'desktop' synchrotrons have been demonstrated in a few research settings [23-25], they remain rare and are not the primary drivers for advancements in grating technology. Figure 1a illustrates a classic Talbot-Lau interferometry system used for X-ray phase contrast imaging [4]. It consists of an X-ray tube as source, a first absorption grating (G0) to create spatial coherence, a phase grating (G1) to generate the interference pattern, and a second absorption grating (G2) to help analyze the fine fringes from the interference pattern, whose pitch can be much smaller than the pixel size on the detector. By displacing, for instance, the G2 grating within one period of the interference pattern formed by G1, a sinusoidal intensity variation is recorded at each detector pixel. This process is known as phase stepping [26]. By comparing the sinusoidal curves recorded with and without the sample (Figure 1b), the three most important signals can be extracted (Figure 1c). The attenuation is obtained from decrease of the average intensity (B_s/B_f). The differential phase contrast is obtained from the phase shift at each pixel ($\Delta\varphi$). The small angle scattering, also referred to as the dark field signal, is obtained from the decrease of the visibility (A_sB_f/A_fB_s). XGI can also be realized with other methods with respect to the one described in Figure 1. For example, dual-phase grating interferometry avoid the use of absorption G2 gratings [27-29].

Due to the long-standing challenge of fabricating high aspect ratio micrometer and submicrometer structures (AR larger than 50:1) in heavily X-ray absorbing materials, high quality diffractive optics have largely been unavailable for hard X-rays and remain a principal bottleneck for commercialization of XGI imaging technique. While silicon remains the dominant material for fabricating these gratings owing to well-established microfabrication processes, alternative materials such as diamond have recently garnered interest [30-33]. Diamond offers exceptional mechanical stability, high thermal conductivity, and outstanding radiation hardness, which make it particularly suitable for demanding experimental environments such as X-ray free-electron lasers (XFELs), which have brilliance values a billion times higher than that from conventional synchrotron, and microstructured array anode sources, where G0 is integrated in the tabletop X-ray source. The unique properties of diamond gratings help overcome some limitations of silicon, expanding the capabilities and robustness of grating-based X-ray interferometry. So far, reactive ion etching of lithographic patterned diamond [33] is still the manufacturing technology achieving the highest aspect ratio in diamond gratings, with an approach very similar to what described here for silicon.

The overall quality of the gratings plays a vital role in the XGI imaging systems [11, 34]. Table 1 lists some of the key control metrics in X-ray grating fabrication and how they affect XGI performance. The impact of grating line profiles as well as related defects has been recently analyzed in detail, including validation by optics simulations with XGI experimental data [14].

Table 1: List of key X-ray grating quality control metrics and their relevant effects on the performance of XGI imaging systems. A schematic illustration of these attributes and defects is provided in Fig. 9 (Section 2.2).

Control metrics / Common defects	Effect on XGI performance
Grating period	Angular sensitivity, signal to noise ratio
Grating duty cycle	Sensitivity, signal to noise ratio
Lamella height	Effective X-ray energy, visibility
Pattern uniformity	Visibility, phase map uniformity
Grating area and bending	Field of view, visibility uniformity
Density of metal filling	Effective X-ray energy, visibility

1.2. Grating Fabrication

Fabrication of high-aspect-ratio silicon micro- and nano-structures is a key process in many applications, including microelectronics [35], microelectromechanical systems [36, 37], sensors [38], thermoelectric materials [39], battery anodes [40], solar cells [41], photonic devices [42] and X-ray optics [26]. A number of microfabrication approaches create a low X-ray absorbing template which is then coated or filled with highly absorbing material. Historically, the templates are based either on polymer [43, 44] or silicon[45].

Although most recent work on X-ray gratings is based on silicon micromachining and DRIE, LIGA (from the German Lithographie, Galvanoformung, Abformung, meaning lithography, electroplating, and molding) has also been explored as an alternative approach and is briefly summarized here for completeness [43, 44, 46]. The LIGA process combines deep X-ray lithography with electroplating to fabricate high aspect ratio metallic structures. It was among the earliest methods used to demonstrate X-ray phase gratings and offers excellent verticality and material absorption properties. However, limitations such as the requirement for synchrotron radiation, challenges in achieving uniform large-area structures, and restricted aspect ratios (around 10:1 for a pitch of 1.2 μm [47]) have limited its wider adoption for grating interferometry. Nevertheless, LIGA remains one of the most advanced microfabrication technologies and continues to be applied where its unique advantages are beneficial.

In contrast, silicon microfabrication is a well-developed technology in the manufacture of integrated circuits and micro electromechanical systems (MEMS) for the semiconductor industry. This gives it the advantage of well-assessed technologies for competitive mass production including deep reactive ion etching [48] and wet etching [49, 50]. The combination of these technologies with unconventional processing methods, along with the flexibility that comes from operating outside the strict design rules of microelectronics manufacturing, has expanded the range of capabilities and significantly contributed to advancements in nanotechnology [51]. With respect to X-ray LIGA, microstructures in monocrystalline silicon are usually also more stable than those in polymer,

so comparatively higher aspect ratios and smaller pitches are achievable in silicon templates. In fact, silicon-based microfabrication produces both robust and very high aspect ratio templates with dimensions below 1 μm. Additionally, the scale-up of substrate size is comparatively straightforward given that commercial manufacturing tools, including for deep reactive ion etching, are commercially available for 300 cm wafers used by the microelectronics industry. Periodic linear gratings with pitches in the range of 100 nm can be patterned at wafer scale by either maskless interference lithography [52] or mask-based displacement Talbot lithography [53], and nanoimprinting processes can be implemented to further increase the patterned area with nanoscale resolution [16, 54]. In addition to polymer- and silicon-based templates, metallic glasses have been explored as imprint materials for high aspect ratio grating fabrication. Owing to their amorphous structure and relatively low glass transition temperature, bulk metallic glasses can be thermoplastically deformed with high fidelity, allowing sub-micrometer resolution over large areas. Metallic glass imprinting has been successfully used to fabricate X-ray gratings with aspect ratios exceeding those achievable with conventional polymer imprinting, demonstrating good mechanical stability and durability [55, 56]. This method offers a complementary route to high performance gratings, it requires a silicon etched template as master and its application remains limited compared to silicon DRIE. From the fabrication point of view, silicon technology is mature and already scaled in mass production and large areas. However, there are unique features of grating manufacture and quality that are not shared by other fields of silicon-based microfabrication. In particular, grating manufacture requires etching technology capable of pattern transfer into the substrate with high control of feature size as a function of the aspect ratio and minimal deformation of high aspect ratio lamellae. Recently reported results indicated that π-phase shift could be introduced to an X-ray with energy of up to 31 keV directly by Si gratings with periods of 1.2 μm and up to 180 keV for gratings with period of 9.92 μm [57]. Figure 2 presents the calculated grating height as a function of X-ray energy for π-phase-shifting Si gratings and absorption gratings, with symbols indicating the grating heights and pitches reported in recent works.

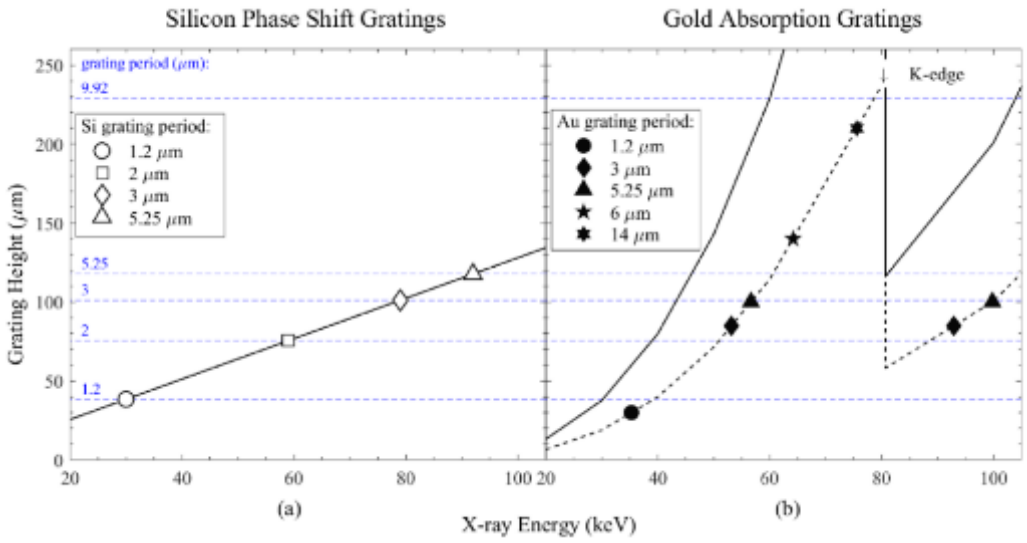

Figure 2: Required grating height as a function of X-ray energy for (a) π-phase shift gratings and (b) assuming Au-filled Si templates. Symbols indicate fabricated (a) Si gratings in [57] and (b) Au-filled Si DRIE gratings in [58-61]. with different pitches. Photon intensity reduction is shown for 1/e (dotted line) and $1/e^2$ (solid line) absorption levels. Horizontal dashed blue lines in (a) and (b) are useful to find the corresponding operational X-ray energy (b) if the Si gratings in (a) are filled with Au. A Si grating with pitch 9.92 μm and height of 231 μm is also indicated, its π-phase shift energy is out of the scale. For clarity, absorption grating data points are shown only on the 1/e curve. Figure reproduced with permission from [57].

Beyond XGI, reflection gratings, for example, are widely used in synchrotron and laboratory-scale spectrometers, where they provide high spectral resolution across the soft X-ray to EUV ranges, they are usually blazed periodic structures etched in silicon at low aspect ratio [62]. Transmission gratings also play a critical role in monochromators for beamline instrumentation, enabling wavelength selection and spectral purity in synchrotron facilities. In addition, large-area transmission gratings are essential for space-based X-ray astronomy [63, 64]. These critical-angle transmission (CAT) gratings are submicron periodic free-standing and silicon lamellas with aspect ratio in the range of 40-60 [63, 64] and have been developed to achieve high-resolution spectroscopy of astrophysical sources. The methods currently used for fabrication of reflection gratings, such as diamond ruling [65] or more advanced anisotropic wet etching of miscut <111> Si wafers [66, 67], reactive ion etching [68], through mask oxidation [69] and others are essentially different from the those used for high aspect ratio transmission gratings and are out of scope of this review. The present review focuses on transmission gratings fabricated using deep reactive ion etching for X-ray phase contrast imaging, these other applications highlight the wider technological importance of grating fabrication methods in X-ray Optics.

Beyond X-ray applications, high aspect ratio gratings are also required in neutron grating interferometry, particularly for thermal neutrons (neutrons with a kinetic energy of about 0.025 eV). The fabrication strategies are closely related to those developed for X-ray Optics,

with deep reactive ion etching of silicon playing a central role. Early demonstrations of silicon-based neutron gratings established the feasibility of DRIE for this purpose [70]. Like in case of X-rays, Si high aspect ratio gratings can be used as phase gratings also in case of neutrons [71-73]. Gadolinium is used as absorption material for neutrons. Tilt-evaporation [70, 71], particles filling [74], metallic glass imprinting [75, 76], and laser ablation [77] have been reported as methods to create absorption gratings. Including neutron gratings highlights the broader applicability of DRIE-based processes for fabricating high aspect ratio periodic structures across different types of penetrating radiation.

1.3. Silicon-based grating fabrication

The process flow generally includes three main steps (Figure 3): 1) the grating pattern is prepared on the silicon substrate with a lithography step; then 2) the pattern is transferred into the silicon using an etch process; finally, 3) the deep trenches formed in the second step are filled with highly absorbing materials. For each step, there are various methods to choose from, depending on the specifications from the grating design, such as the period, height, material.

Patterning is usually accomplished using a lithographic method that can be mask-less (direct writing) or involving the use of a mask (mask lithography) or a master (nano-imprint lithography). It involves the use of a radiation-sensitive polymer resist that can be patterned with the grating design through the modified chemical reactivity of the exposed resist.

Etching can be accomplished by dry methods involving a plasma [57, 60, 78-82], anisotropic wet solutions [45, 49, 83] or catalyst-based metal-assisted chemical etching [42, 51].

The metallization step comprises electroplating [59, 84-86], metal casting [87, 88], atomic layer deposition (ALD) [89], or centrifugal deposition [80, 90].

The flexibility of the Patterning-Etching-Metallization approach, with the multiple methods available for each step, makes silicon-based fabrication more widely accessible to research groups working on grating-based X-ray imaging technologies [79]. In Figure 3, it is seen that, by going through only the first two steps, a silicon-based phase grating can be produced; adding the third ‘metallization’ step allows fabrication of absorption or phase gratings for higher X-ray energies. A more advanced method to further increase the aspect ratio of the grating is the double-side grating fabrication technique [50], which has grating structures embedded in both sides of the silicon wafer. This relies highly on the alignment accuracy of the lithography system, as well as having additional potential challenges for using such gratings in X-ray experiments. Bendability of double side patterned gratings may also be limited by the tensile stress induced closer to the outer (convex) surface, especially if the grating is intended for use as the G0 grating located in front of the source, where bending radii of several centimeters are needed.

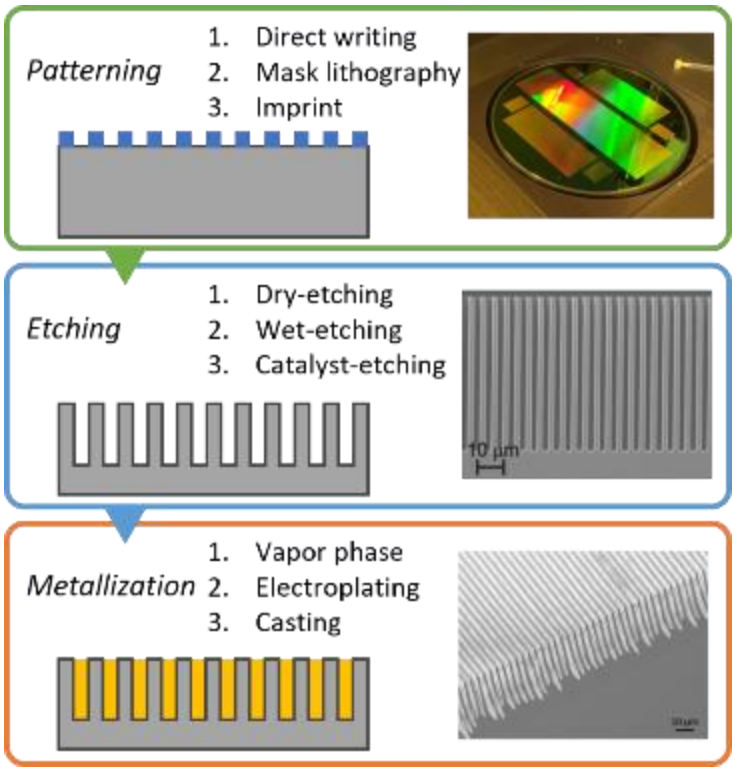

Figure 3: Schematic of the Patterning-Etching-Metallization process flow for preparing high aspect ratio metallic microstructures with silicon template. There are multiple methods to accomplish each step; only a few examples are listed here. Original figures by the authors are provided to support the concept.

The definition of the area to be etched involves the preparation of a grating pattern on the substrate. Various lithography methods can be selected based on the grating design, with each presenting its own advantages and drawbacks. Direct writing methods are often distinguished by high resolution. Electron beam lithography (EBL) [21] has a longstanding history of application in grating pattern preparation [91, 92] and mask fabrication [93]. It remains widely employed for prototyping novel X-ray optics designs, especially for nanometer-scale grating periods [94-98]. Its primary limitation lies in process speed, with writing times ranging from many hours to days or even weeks for gratings of tens of cm^2 in size. Additionally, the photoresists for EBL, even the ZEP-series 'etching-photoresist' [99], are not resilient enough for deep reactive ion etching (DRIE) processes. Direct laser writing (DLW) [100], by contrast, does not require vacuum and offers faster exposure speeds [101, 102], making it feasible for producing large-scale gratings with micrometer-scale periods. However, DLW remains time-consuming for extra-large gratings or for mass production when sub-micrometer periods are required. Mask-based lithography has fast processing time (minutes) and is more suitable for batch production. Conventional UV-lithography with a mask aligner offers a swift process by directly projecting the entire grating pattern onto the silicon substrate [89]. This method is most convenient for gratings with relatively large

periods; the resolution is limited, typically at about 1 µm pitch, with the linewidth uniformity over large areas potentially problematic, which is a critical issue in grating fabrication [53]. This arises from the fact that any imperfections or defects present on the wafer surface induce non-uniform UV light scattering, attributable to variations in the mask-to-wafer spacing during the contact mode exposure used for the highest patterning resolution. As an interference lithographic method, Displacement Talbot lithography (DTL) provides a non-contact exposure process [103], ensuring uniform line width roughness across the entire wafer with a large depth of focus [53]. Leveraging the interference pattern generated with a laser source and a photomask, DTL proves particularly effective for creating periodic patterns with pitches ranging from a few micrometers down to about two hundred nanometers [15, 104, 105]. Nanoimprint lithography has demonstrated its efficacy as a viable technique for generating patterns featuring sub-micrometer critical dimensions across extensive areas [106]. This approach has been employed in the production of high-quality blazed diffraction gratings, including for synchrotron beamline applications [107] and for astrophysical soft X-ray spectroscopy [107, 108]. To prevent the degradation of the costly master, a preventive measure involves the application of a sacrificial medium layer [16], which effectively preserves the high fidelity of this method. However, nanoimprint has very high surface cleanness and wafer flatness requirements, which affects the robustness of the method, especially when it comes to serial production.

The lithographic step is often accompanied by an additional hard-mask preparation step to transfer the pattern into more etching-resistant materials [84]. In a plasma etching process, the hardmask acts as a protective layer and exhibits high selectivity compared to the target etching material. There is a wide selection of materials suitable for hardmasks, including silicon nitride [109], silicon oxide [110], aluminum oxide [111], and metals such as aluminum [112] and chrome [113]. The process of transferring the etching pattern from photoresist to the hardmask and then into the substrate is shown schematically in Figure 4. Details of associated processes can be found in the literature [95, 114].

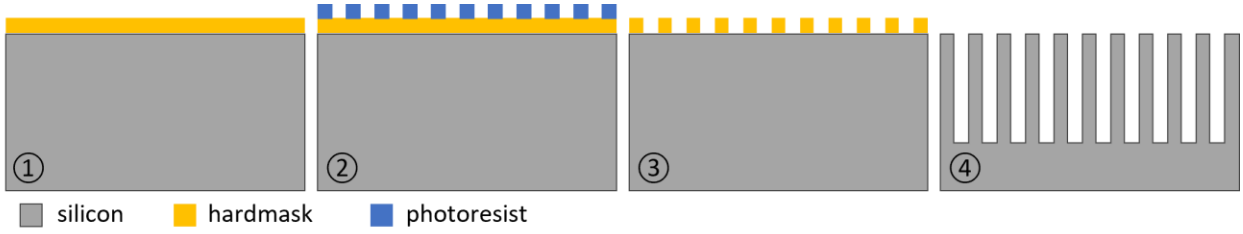

Figure 4: Schematic of pattern transfer from the photoresist to the hardmask. 1. Deposition of the hardmask material. 2. Lithographic patterning of the photoresist. 3. Etching of the hardmask using the photoresist layer as the etching mask. 4. Final silicon DRIE step using the hardmask as the etching mask (shown after its removal).

1.3.2 Silicon etching

High aspect ratio pattern transfer is usually achieved by plasma etching [115]. A high etching rate with low dependence on aspect ratio is crucial for good profile control during deep reactive ion etching [57], which is described in details in section 2. Wet-etching in alkaline solutions [45, 116] has been used for microfabrication as a less expensive technology. However, the aspect ratio is limited by the ratio of the etching rates of different crystallographic orientations and only possible in simple geometries like linear gratings or crossed linear gratings defined by the direction of the <111> crystallographic planes of silicon. For gratings fabricated on (110) silicon wafers, the crystallographic directions must be aligned with the lithographic pattern orientation, i.e., correspondence of the <111> orientation on the wafer surface and the direction of the grating lines, to suppress transverse etching that otherwise limits the achievable aspect ratio and duty cycle (Si line width/pitch, DC)[117]. Established procedures such as the wagon wheel method are commonly used for this alignment [118]. In addition, KOH etching has been applied after DRIE as a polishing step to improve sidewall quality and reduce surface roughness [119], particularly in the context of critical angle transmission (CAT) gratings developed for astrophysics [120]. Examples of wet-etched gratings are shown in Figure 5 [49, 117]. Limited selectivity between the etching rates of crystallographic planes in Si results in a reduced duty cycle of ~0.28 [49]. Moreover, the etching depth is subject to increasing non-uniformity with increasing aspect ratio due to trapping of hydrogen gas by-products at the undercut beneath the mask [49].

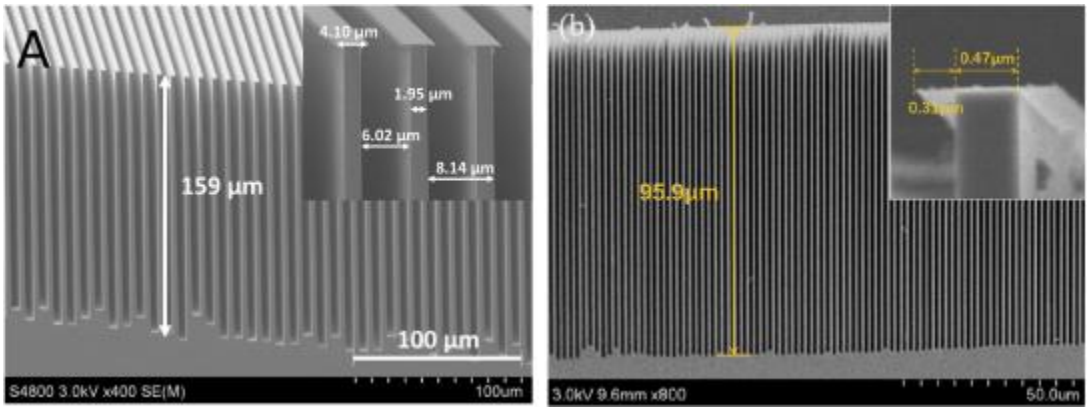

Figure 5. Examples of Si gratings produced by KOH wet-etching, cross-section SEM images reproduced with permission from ref. [49] (left) and [117] (right).

Another approach for anisotropic wet etching of Si is photo-assisted and voltage biased electrochemical etching [121]. Pits are first etched into the Si surface in an alkaline KOH solution. These pits are then extended into the underlying substrate through a combination of rear and front surface illumination to generate minority carriers and a biasing electrical field within the wafer in an acidic HF solution to localize etching to the feature bottom. Using this method 1.5×1.9 μm^2 holes were demonstrated to a depth of 150 µm [122].

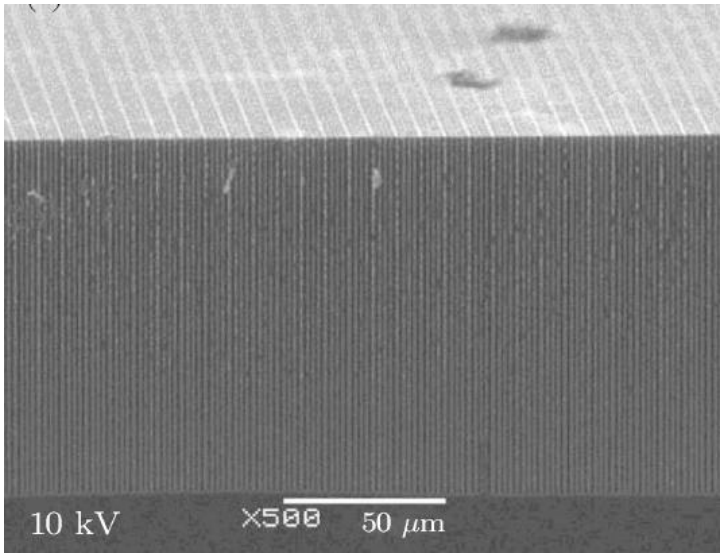

Figure 6. A grating with 1.5×1.9 μm^2 rectangular holes in a periodic multi-pore pattern etched to a depth of 150 μm by electrochemical etching, reproduced with permission from ref. [122].

As an alternative approach, metal assisted chemical etching (MacEtch)[123] has attracted great interest [121, 124-126] because it is a plasma-free, low-cost, and scalable method [48] to produce high aspect ratio structures across widely different dimensions [127, 128]. In the MacEtch process, a metal catalyst (e.g., Pt, Au or Pd) promotes localized reduction of H_2O_2 that, coupled with hole transfer to the Si substrate, promotes oxidation and removal of Si in an HF acid solution. The catalyst descends into the substrate with the Si removal enabling a continuous etching reaction. Unlike conventional alkaline wet-etch [116], the MacEtch process is almost independent of crystal orientation. It also may be used to create a wide variety of patterns without suffering from the micro-loading effects of dry-etch processes [51, 105, 129-132]. Further, although the method offers considerable reduction in fabrication costs and complexity with respect to the other techniques, demonstration of good uniformity over large areas of MacEtch fabrication is still limited, in part by a lack of commercial tools. An example of a Si grating realized by MacEtch is shown in Figure 7.

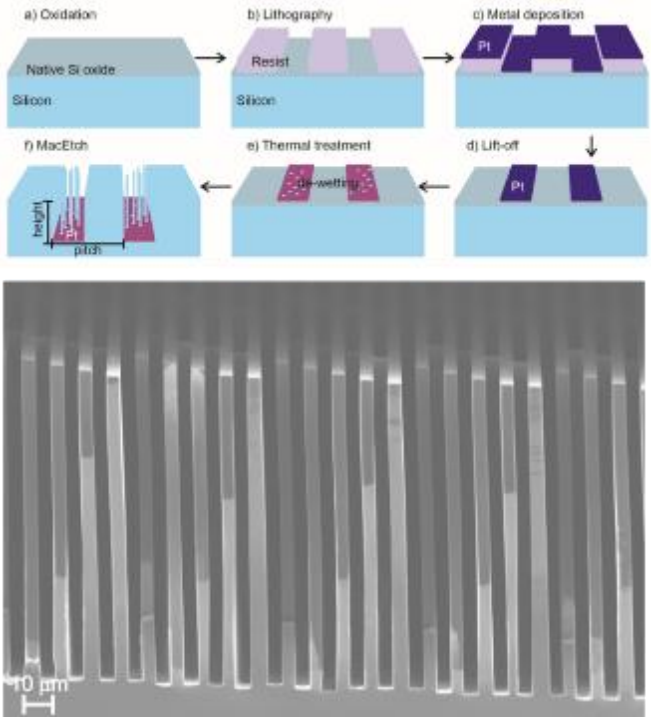

Figure 7. Schematic of MacEtch process for Si gratings; cross-section SEM image (grating with pitch 10 µm and trench depth of 110 µm), reproduced with permission from ref. [131].

2. Silicon Deep Reactive Ion Etching

Among the many variants of the Patterning-Etching-Metallization process flow, for the etching step, deep reactive ion etching (DRIE) has the advantage of good uniformity over large areas and wafer-to-wafer repeatability at a reasonable process cost. Indeed, the DRIE method has a proven track record for the production of high aspect ratio microstructures [133]. However, there are intrinsic limitations in silicon DRIE. This review paper discusses the main challenges, detailing how the DRIE method can be optimized in the Patterning-Etching-Metallization protocol for the fabrication of X-ray gratings.

Deep reactive ion etching (DRIE) of silicon has been extensively studied due to its critical role in applications including very large-scale integration (VLSI) and microelectromechanical systems (MEMS) [134]. Broadly speaking, such plasma etching processes are complex, involving both physical bombardments from ions and chemical reactions with etchants [135]. Given the strong chemical bond in silicon, dry etching of silicon demands a high etchant density [1]. Consequently, inductively coupled plasma (ICP) etching systems, which offer a higher ionization rate compared to capacitively coupled plasma (CCP) systems, are commonly used for silicon DRIE. A commercial ICP system typically includes a

power supply to ignite the plasma and continuously ionize the etchant gas, as well as a radio-frequency (RF) power supply to increase the bias voltage (Figure 8a) [135]. Some ICP etchers feature multiple sets of ICP or RF power supplies, leading to improved etching uniformity through more evenly distributed etchant density [136].

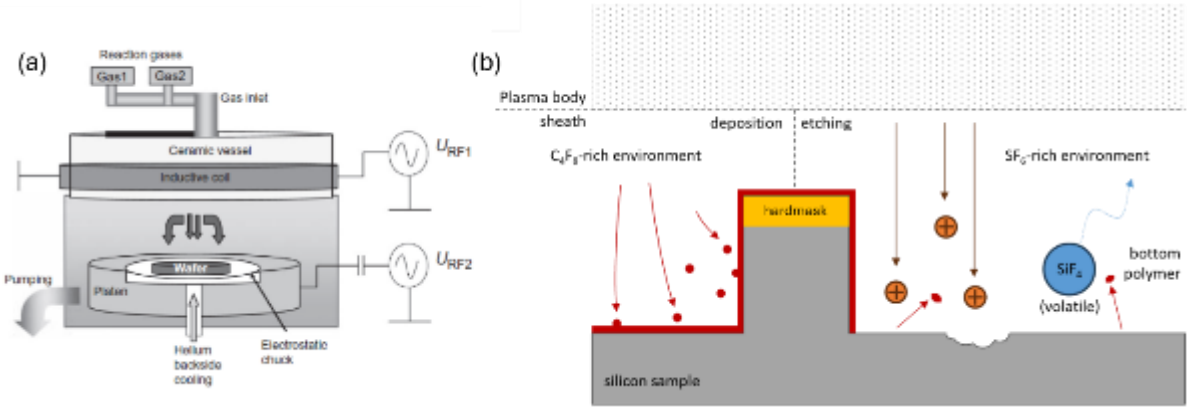

Figure 8: (a) Schematics of an ICP etching system, reproduced with permission from ref. [137]. (b) Schematics of silicon etching mechanism (Bosch process) by radicals.

While the physical impingement and mass removal in plasma etching gives the process a directional nature, lateral etching from chemical reactions limits the achievable aspect ratio. The Bosch process addresses this limitation by alternating the etching steps with deposition sub-steps that form protective polymer layers on the trench sidewalls, facilitating the etching of deeper trenches [138]. The etching step commonly employs SF_6, which breaks into fluorine-based radicals that etch silicon isotropically. Fluorocarbon radicals are then created in the second step by breaking up C_4F_6. These radicals deposit as a robust polymer, stable below 50 °C, on the sidewalls of the etched surface [139]. Termination of the etching process occurs when the required depth is reached or the etching mask is fully consumed. To maximize the achievable aspect ratio with a limited hardmask thickness, precise estimation of the instantaneous etch rate is crucial to avoid overconsumption of the hardmask. A modified Coburn-Winters model describes aspect-ratio dependency with a simplified Knudsen coefficient $K = ln(\alpha)/\alpha$, where K is the Knudsen coefficient and α is the instantaneous aspect ratio of the deeply etched trench [57]. Advanced Bosch etching processes further refine the etching sub-steps, initially removing polymer protective layers at a higher bias voltage and then reducing the bias voltage once the silicon material is exposed again. This conserves the etching mask even as it decreases sidewall roughness [140]. Extending the DRIE process to create deeper features can be accomplished by increasing the thickness of the hardmask and/or using a hardmask with higher selectivity to etching versus the underlying substrate.

Defects including scallops, tapering, bowing, and microloading are characteristic markers of Bosch processes in etched microstructures [135]. As defects, they reduce the quality of the etched profile and negatively impact the performance of the gratings. A detailed presentation of commonly observed Bosch defects, together with strategies for mitigating them, follows.

The crucial specifications of an X-ray grating extend beyond the aspect ratio of its features. No less importantly, their profiles play a significant role in the performance of the imaging system in which they are integrated. Ideally, both phase shift and absorption gratings should feature perfectly rectangular-shaped grating lines. However, current micro-fabrication technology limitations compel researchers to navigate the different defects, including a trade-off between aspect ratio requirements and profile control. Key parameters are schematically illustrated in Figure 9a:

- Pitch (p): the grating's period.
- Duty cycle: a/p and b/p, where 'a' and 'b' are the Si line width at the top and bottom of the trench, respectively.
- Average etch rate: calculated by measuring the etch depth (h_1) at the end of the etching process.
- Selectivity: the ratio between the etch rates of silicon and the hardmask.
- Sidewall angle (α): the degree of tapering, calculated by $arctan((b - a)/2h_1)$.
- Bowing: for gratings with a given pitch and height, described using the thinnest part of the silicon lamellae (denoted as 'c' in Figure 9a), frequently in terms of the average width

Figure 9b-g show SEM images of cross-sectioned gratings that illustrate the typical Bosch-defects. The profile of the trench is extremely important for the X-ray imaging applications since the optimal duty cycle (DC) for XGI is in the range of 0.4 to 0.5 [141]. Variation of the Si line width as a function of depth (e.g., a, c, b in Figure 9a) translates into a modulated X-ray intensity profile through the grating, with non-obvious impact on performance of the XGI system in terms of visibility, sensitivity and dose efficiency [14].

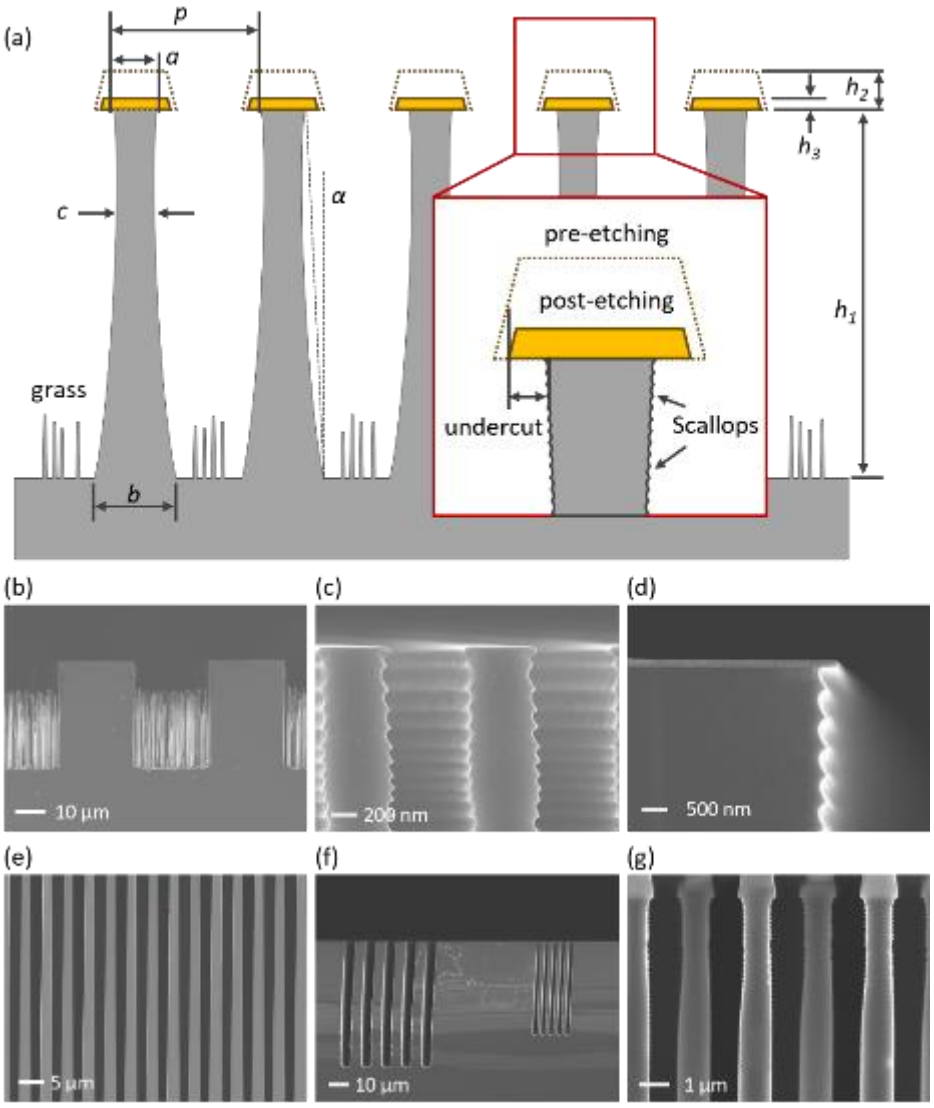

Figure 9: Typical defects in a high-aspect-ratio grating fabricated by DRIE [1]. In the schematic (a) with etch depth denoted as h_1, the hardmask consumption is labelled as h_2. The upper duty cycle is defined as a/p while the bottom value is defined as b/p. The thinnest linewidth, c, is used to describe the severity of bowing. The sidewall angle is denoted as α. Example SEM images of (b) grass, (c) scallops, (d) undercut, (e) taper, (f) loading effects (i.e., variation of etch depth with feature size and density), and (g) bowing. Reproduced with permission from ref. [1].

2.1 Etching features

2.1.1 Grassing

Formation of silicon nanowires in etched trenches, aka "grass", is a consequence of random micro-mask formation in the exposed area. The schematics in Figure 10 show two of the major causes of micro-masks formation. Sputtered and relocated hardmask material can serve as micro-hardmasks [137, 142-144] that lead to the formation of silicon grass. Alternatively, insufficient polymer removal from the bottom surface can also create micro-hardmasks [137, 145, 146]. Together, these mechanisms explain why the grassing is often observed during the fabrication of gratings that have larger periods (>10 μm) or using metal hardmasks. Even in a mask-free plasma etching process, local non-uniformity in etching behavior can create a grassy surface, which has a direct application in black silicon production [147, 148].

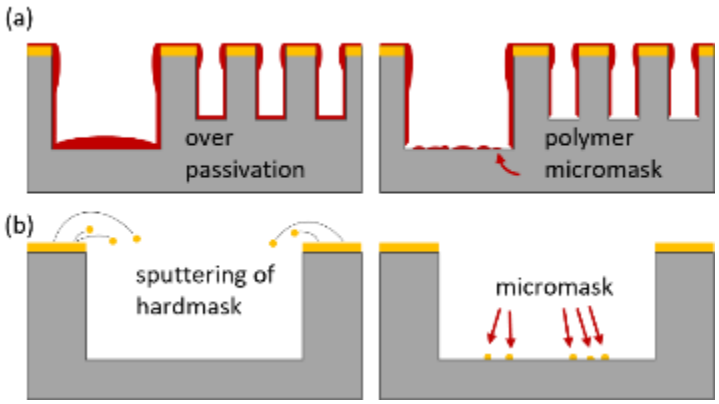

Figure 10: Two possible mechanisms for the formation of grass defects. (a) Thicker polymer protection layers can form inside trenches with larger openings; incomplete removal of the bottom polymer during the etching steps leaves residue that acts as micro-masks. (b) The plasma can sputter and re-deposit hardmask material from the field that serves as micro-masks at the bottoms of the trenches.

Depending on the density of these defects, grass can produce X-ray scattering and contribute to the noise of an XGI imaging system; a low density of the defects might be tolerated in G1 gratings, barring impact on the subsequent metal filling step. They can be moderated, or eliminated, using several different approaches. For example, some mask materials with moderate selectivity (such as SiO_2 or Si_3N_4) form volatile products of reaction with plasma such that they are less likely to form micro-masks in a plasma etching process. Grass formation can also be inhibited by increase of the etching-to-deposition ratio [149] or higher bias voltage to ensure that byproducts are fully removed from the trench bottoms. Alternatively, grass structures can be removed with mild post-process (e.g., SF_6/O_2 plasma

treatment, short KOH etching, etc.) after the etching is otherwise completed. However, formation of the small and high aspect ratio grass structures generally marks the limit of the maximum achievable etching depth.

2.1.2 Scalloping

Scalloping refers to the periodic roughness that can be observed on the sidewalls of Bosch-etched microstructures [150]. Its formation is inevitable given the iterative use of etching and deposition steps in Bosch etching processes. In particular, the plasma etching process is a combination of chemical reaction between the etchant and the sample material and the physical bombardment of the positively charged ions from which a certain level of isotropic etching is expected. Figure 11 schematically explains the formation of the scallops during a Bosch etching process, although the actual result is generally more complex [151]. Typically, scallops are in the range of 80 nm to 120 nm in size, but they can be much larger depending on the parameters of the etching recipe [152-154]. Like modest grass formation, scallops do not typically affect grating performance in XGI meaningfully, particularly if the period of the gratings is relatively large (e.g., 2 μm). However, when the period of the gratings is small, e.g., sub-micrometer, then the impact of scallops can be non-negligible. Approaches similar to those used for grass removal can also be applied to smooth the sidewalls of the trenches [140, 155]. Scallops predominantly affect the upper part of the trench profile, as shown in Figure 9c, d. This is because the upper sidewall is more exposed to the etching plasma and the ions can hit the sidewalls at large incident angles yielding comparatively fast removal of material. In contrast, the ion trajectories are progressively more parallel to the sidewalls farther down the trenches, yielding a smoother surface [156]. Aspect ratio dependent etching also influences the scallop profile; as the aspect ratio of the etched trench increases, the convection of the gases and removal of etch byproducts becomes less effective, stabilizing the polymer on the sidewall, which further decreases the scallop size and contributes to the smoother appearance of the sidewalls [157].

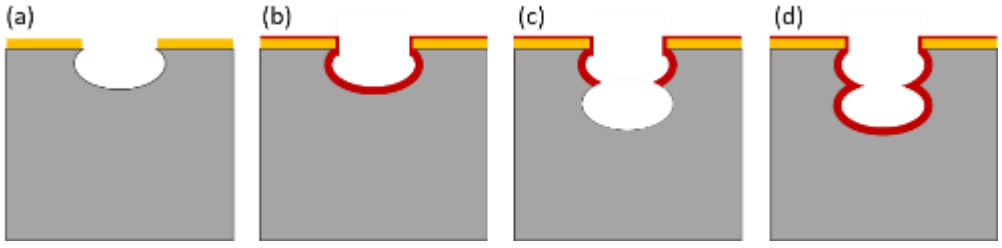

Figure 11: Formation of the characteristic scalloped profile from a Bosch etching process. (a) Trench profile after the first etching step, (b) the sidewall and the bottom are protected with a layer of polymer after the first deposition step, (c) trench profile after the second etching step, that begins with removal of the polymer layer at the bottom of the volume removed during the first etching step, and (d) trench profile after the second deposition step.

2.1.3 Undercut

Undercut is associated with the first 'scallop' feature under the hardmask and is usually deeper (more recessed in the sidewall) than the other scallops. The origin of undercut is still under debate [113, 158-164], but there is general agreement that its severity relates to the hardmask material. Undercut is often described as the difference between the hardmask edge and the width at the top of the silicon microstructure, as shown in Figure 9a; as the hardmask is also consumed laterally during the etching process, increase of the trench opening width is the sum of the undercut length and the hardmask consumption length. Significant undercut is mostly observed with a metal hardmask; it can be moderated using a dielectric hardmask. Silicon nitride hardmask is reported to reduce undercut better than silicon oxide, repelling ions like SF_5^+ from the positively charged hardmask edge [162]. Altering the protective layer is another approach to reduce the undercut [165]. Lowering the process temperature also is effective in minimizing undercut [164]. However, this adjustment concurrently reduces the etch rate and alters the etching profile, so implementation of this approach requires further recipe tuning. Alternatively, one may simply introduce systematic compensation at the lithography step and make the average trench width narrower (or wider) by finetuning the angle of sidewall tilt, as shown in Figure 12.

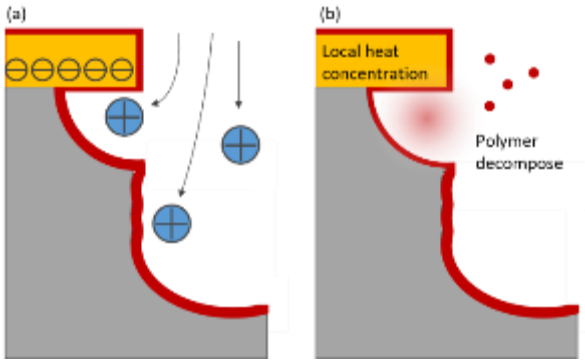

Figure 12: Two mechanisms of undercut formation. (a) A negatively charged attracts the positively charged etchant ions as they approach. (b) The temperature gradient induced by proximity to the plasma convolved with more rapid decomposition of the polymer layer at higher temperature results in a thinner protective polymer layer close to the hardmask.

2.1.4. Tapering

The cross-sections of the trenches (and features more generally) etched into gratings are not always rectangular; they can be parabolic, triangular [166], trapezoidal [167], etc. That said, most X-ray grating designs, especially the phase gratings, have a preferred rectangular profile for the grating lines, which requires the etched trenches to have vertical sidewalls.

This comes with the caveat that with absorption gratings, a slightly tapered sidewall may be introduced to mitigate limitations of the Au deposition process that might otherwise result in voided fill [86]. Whether vertical or tapered sidewall, a well-controlled shape requires a well-tuned plasma etching process [137]. Parameters that can affect the sidewall angle [168] include the etching/deposition time ratio in the Bosch etching process, the RF power setting, the gas flow, the chamber pressure, and temperature. Figure 13 shows schematics of sidewall profiles representing positive, neutral, and negative taper angles as well as experimental examples of the first two [169]. The impact of tapering on an XGI's performance can be seen in Figure 14.

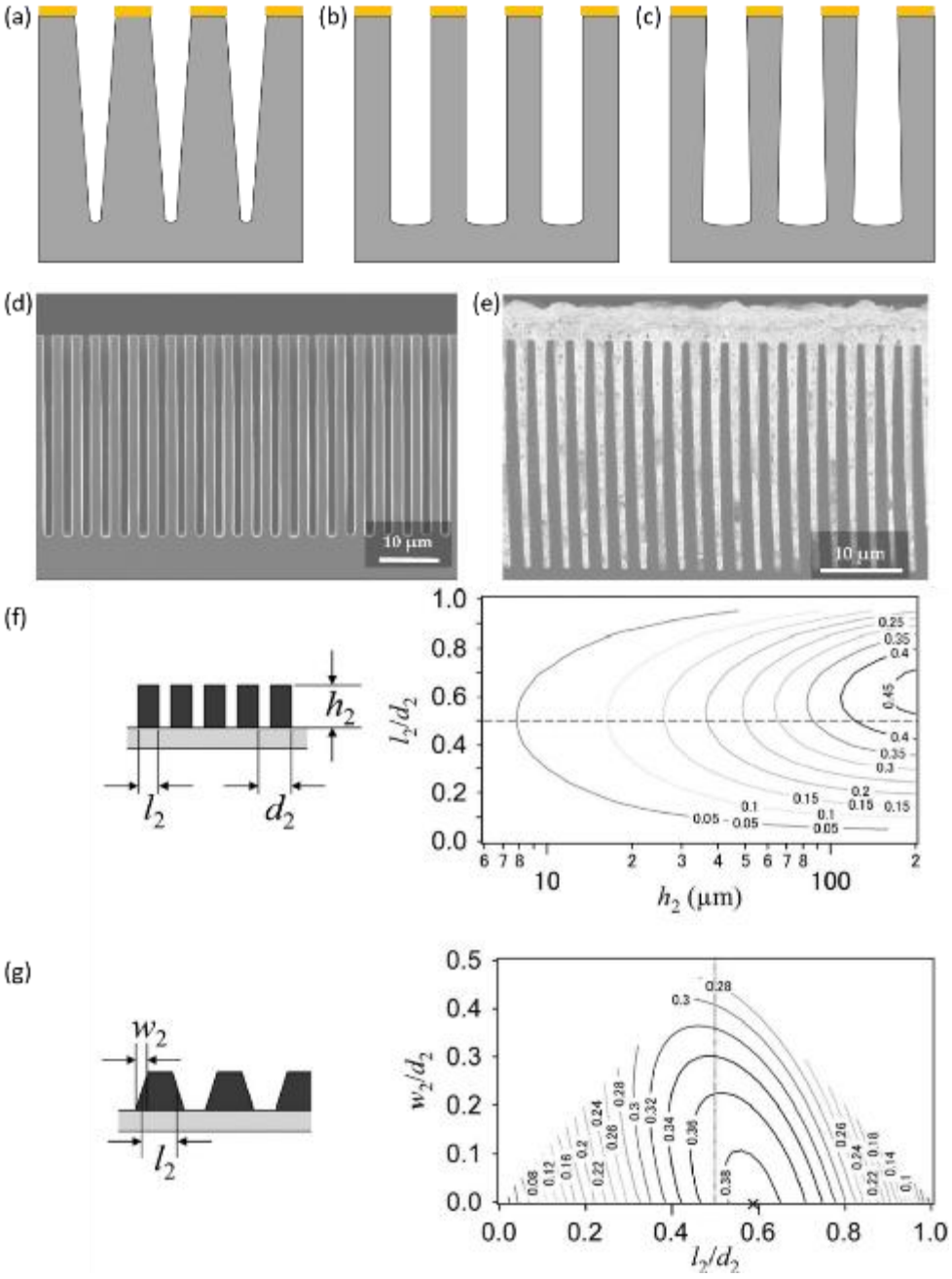
(a)
(b)
(c)
(d)
10 μm
(e)
10 μm
(f)
h_2
l_2
d_2
l_2/d_2
h_2 (μm)
(g)
w_2
l_2
w_2/d_2
l_2/d_2

Figure 13: Schematics of deeply etched trenches that have (a) positive taper, (b) vertical sidewalls, and (c) negative taper. (d) Cross-section SEM image of a silicon grating template that has vertical sidewalls after recipe tuning, and (e) partially voided absorption grating with positively tapered sidewalls after nominally conformal gold electroplating, adapted from ref. [58]. Visibility predicted as function of (f) pattern height and normalized linewidth for a rectangular grating and (g) average linewidth and normalized slope width for a trapezoidal grating with fixed height, adapted from ref. [169].

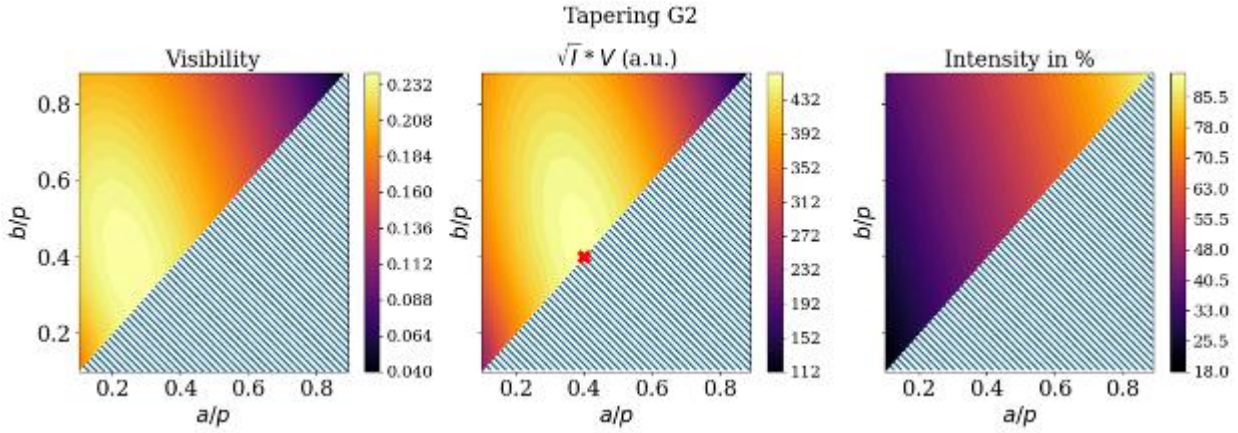

Figure 14: Wave-propagation simulation of a tapered G2 grating for different trench width ratios as defined in Figure 9a. The grating with the highest sensitivity is found at a duty cycle of 40 %. For a fixed mean duty cycle (i.e., $a + b$ constant, moving perpendicular to the diagonal boundary of the simulated region), tapering leads to a moderate change in sensitivity compared to a complete change of the mean duty cycle. Figure reproduced with permission from ref. [14].

2.1.5. Loading effects

Loading effects refer to pattern-density–dependent variations in etch rate caused by (i) local depletion of reactive species in high-density regions and deep trenches and (ii) transport limitations for ions, polymer fragments, and volatile byproducts into and out of features. Loading effects impact etch-depth uniformity (Figure 9f and Figure 15). As such, loading effects depend on exposed area, feature geometry [170] (line trenches, holes or pillars), aspect ratio and density (i.e., pitch) as well as the size [48, 171] of the pattern. Loading effects are reported using different names in reference to the responsible feature [172]. Macroloading is usually in reference to the exposed area. Microloading and ARDE (Aspect Ratio Dependent Etching) or RIE-lag [173] refer to lower etch rates in features with smaller openings because of reduced transport of fluorine radicals as well as more rapid formation of higher aspect ratio recesses during etching. Microloading and ARDE principally result from reduced transport of the etchant ions into the features and polymer particles and volatile byproducts out of the features during the etching step, as shown schematically in Figure 8b. For the fabrication of gratings with periodic patterns the impact of microloading

should be uniform and thus irrelevant. However, non-uniform trench opening width, both locally and over a larger scale [15], for example, as a result of non-uniformity of the linewidth in the etching mask, will result in similarly non-uniform etching depth due to ARDE. Pattern uniformity in the lithography step is key. Where such uniformity is difficult, as when the period of the grating is small, the etching recipe can be tuned to reduce the impact of microloading [173] or even reverse it by attempting inverse-microloading [174] over a limited range of aspect ratios.

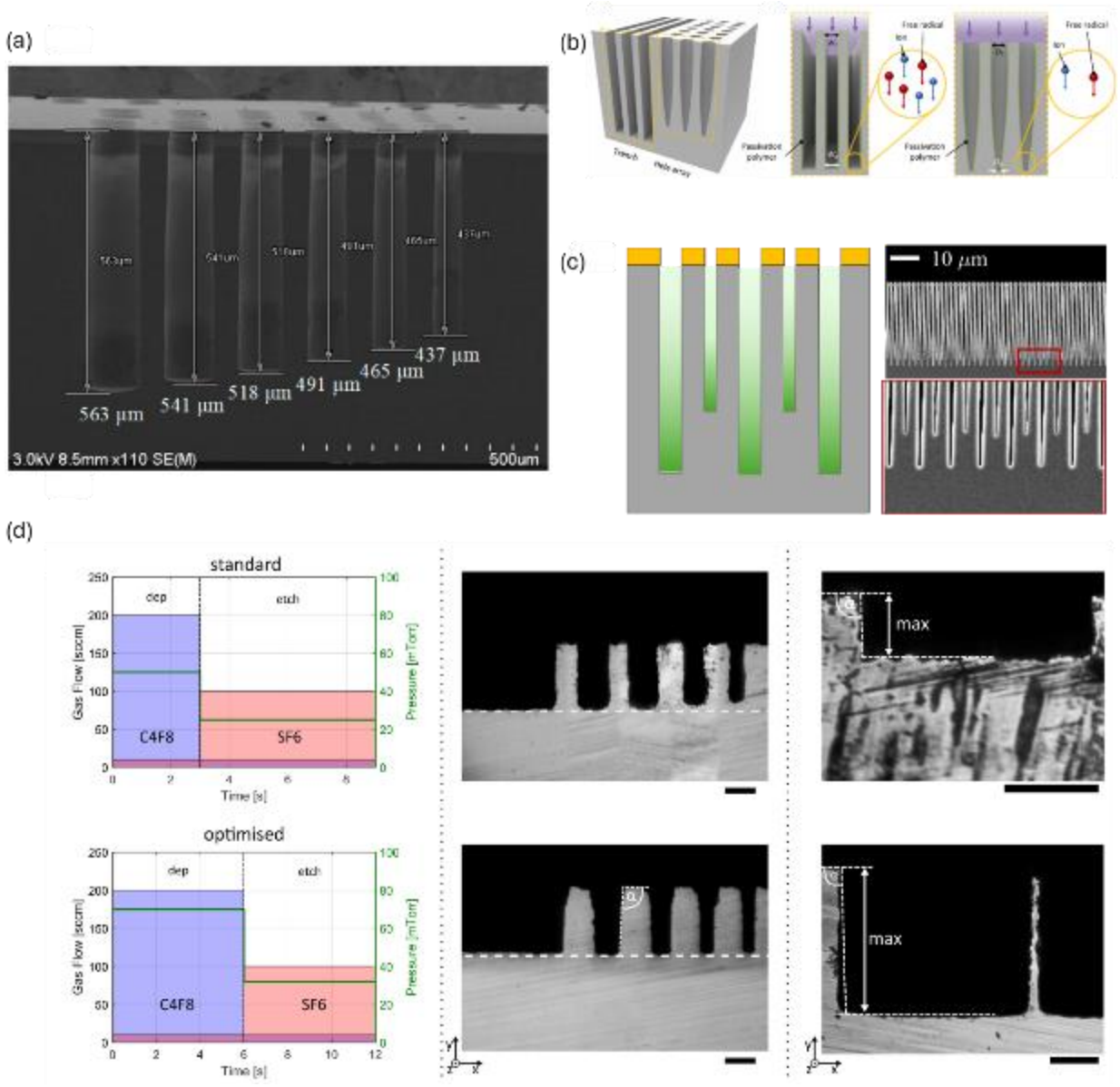

Figure 15: (a) During the deposition step in DRIE, a layer of polymer is first formed conformally on the exposed areas. In trenches with narrower openings, transport of etchant, polymer particles, and byproducts is decreased during the subsequent etching step so that the etch rate is reduced. Reproduced with permission from ref. [171].

(b) Geometrical effects can be understood from the range of angular trajectories for etching ions down the feature permitted by the feature opening. Reproduced with permission from ref. [170]. (c) An example of the resulting microloading effect in a 1 μm pitch grating where the pattern produced by Displacement Talbot Lithography had a linewidth beating defect: schematic and SEM images illustrating that narrower trenches are etched shallower. Insufficient convection of etchants and byproducts as indicated by the color gradient inside the trenches in the schematic is the main reason for microloading effect (Reproduced with permission from ref. [15]). (d) An exemplary approach, with standard and modified etching and depositing gas flow rates and cycle times indicated on the left and reduced microloading evident in nominally uniform etch depth in narrower and wider trenches, reproduced with permission from ref. [173].

2.1.6. Bowing

The phenomenon of bowing in deep reactive ion etching (DRIE) refers to undesirable widening of the trenches at some depth that is observed in silicon and dielectric substrates. Various factors contribute to this defect (Figure 16). For thick hardmasks, a tapered sidewall may reflect ions over specific range of angles, leading to the removal of the flourine-based polymer deposited on the sidewalls. The cyclic sputtering and redeposition of the byproducts can create a non-monotonic profile of width versus depth beneath the trench opening that can itself also serve as an ion reflection source [175]. In whichever location, the exposed silicon undergoes isotropic etching that creates the bowing defect. The distribution of ion incident angles, determined by the bias voltage, can also result in bowing [175] as the distribution pattern means that ions with nonzero incident angles with respect to the perpendicular direction to the wafer surface can still impact the sidewalls, even without the hardmask-derived reflections [176]. During the DRIE process, the sidewalls of deep trenches become negatively charged at the top and positively charged at the bottom [177]. This charge distribution affects the trajectories of etchant ions, contributing significantly to the bowing effect. Significantly, the widening of the trench at the bottleneck, the thinnest part of the grating lines, alters the average duty cycle of the X-ray grating. Further, if the bottleneck narrows excessively, it becomes prone to breakage during etching, necessitating premature termination of the process. Consequently, control of bowing defects is regarded as a critical issue in achieving ultra-high aspect ratio microstructures [1].

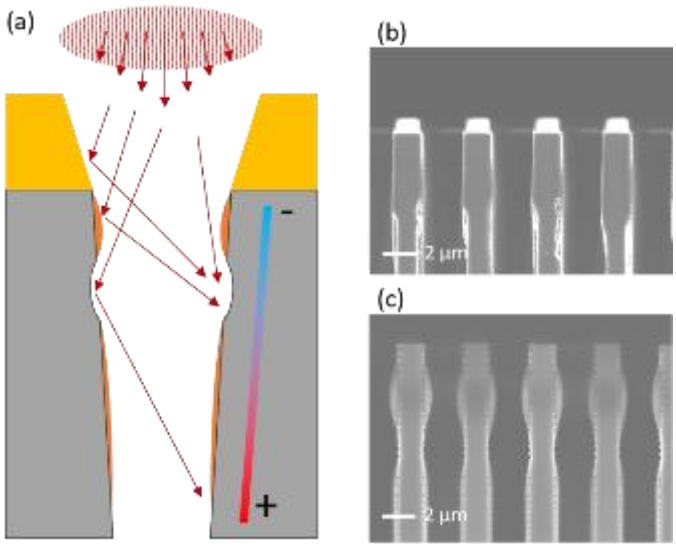

Figure 16: (a) Schematic of some possible causes of bowing defects. For a given ion incident angle distribution, as defined by the etching recipe [175], ions with small incident angle can hit the sidewalls directly [176]. Taper of edge of the photoresist/hardmask can reflect the ions. Excess polymer accumulated at the top of the trench opening, often called necking, can also reflect the incoming ions [175]. Ions with sufficient remaining kinetic energy can experience a second collision with the sidewall. Charging-induced potential variation along the sidewall is another source of ion reflections [177]. Example cross-section SEM images of (b) bowing defect caused by reflections from the tapered photoresist and (c) bowing caused by necking.

2.1.7. Tilt etching

The otherwise undesirable phenomenon of tilted etching, where ion trajectories are altered due to electric field distortions near the wafer edges, has been repurposed for the intentional fabrication of fan-shaped X-ray gratings [178]. In semiconductor manufacturing, this effect typically causes non-vertical etching, particularly in high aspect ratio (HAR) structures, due to plasma sheath curvature. For X-ray optics, this distortion has been intentionally used to create gratings with a progressive tilt from the wafer edge to the center. By modulating the electric field during DRIE processes, ions are made to strike the wafer surface at oblique angles, producing tilted grating profiles that can align with the divergent X-ray beam from conventional X-ray sources [179]. This alignment enlarges the field-of-view (FOV) and imaging uniformity in X-ray interferometry systems. The resulting fan-shaped gratings improve phase contrast and signal-to-noise ratios in X-ray imaging by ensuring more uniform illumination across the field [180]. In the related development of CAT gratings, non-destructive measurement of bar tilt over large areas has been demonstrated [181], and recent work has explored measuring and controlling bar-tilt uniformity across different DRIE platforms [182]. These characterization approaches can be leveraged to assess and optimize the intentionally tilted gratings described in this review.

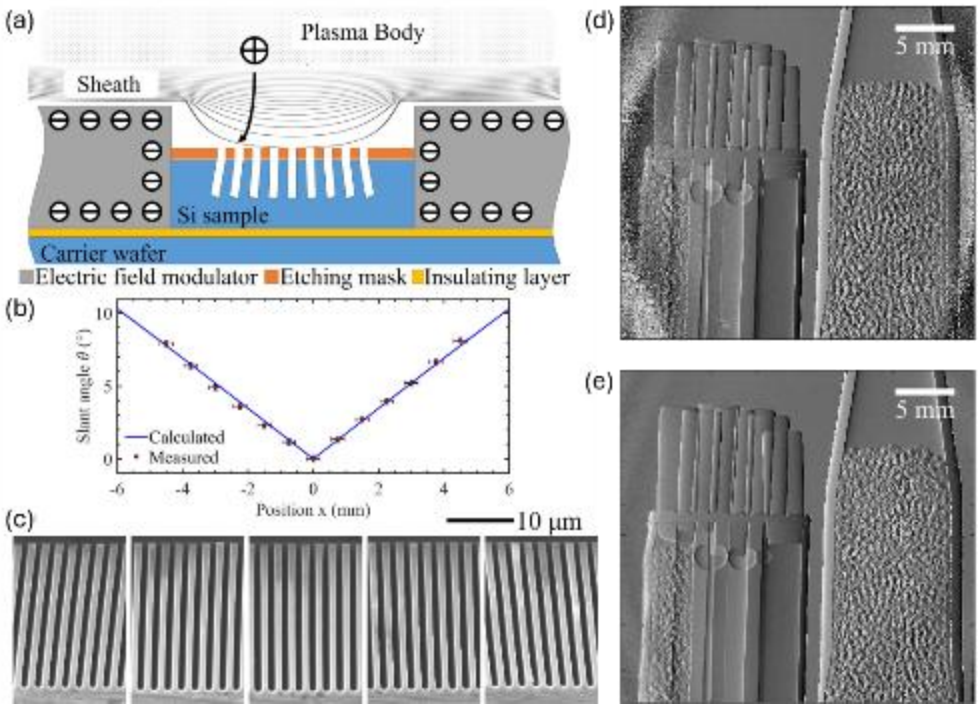

Figure 17: (a) Schematic of the etching process in the presence of electric field modulators. (b) Slant angle as a function of the position from the center in a grating etched with fan-shaped trenches; (c) the angle is measured in SEM images of cross-sectioned specimens at different distances from the center of the grating. Differential phase contrast images acquired with a Talbot-Lau interferometry system equipped with (d) a conventional source grating (i.e., trenches uniformly orthogonal to the field) and (e) a source grating with fan-shaped trenches; contrast is degraded toward the left and right sides with the former. Reproduced with permission from ref. [180] © Optical Society of America.

2.2 Etching Recipe Tuning with Orthogonal Experimental Design Method

Defects are intrinsic to DRIE due to the nature of the process. Fine tuning of etching recipes to avoid or minimize specific types of defects plays a crucial role in processing engineering. There is no 'golden rule' in plasma etching, as each of the key parameters can have multiple side effects on the etching profile. Thus, for example, correction of a tapered profile in deeply etched trenches by increasing the etching/deposition ratio sacrifices selectivity. The cross-effects of parameters in plasma etching makes the control variates method that is commonly used for tuning processes [137], ill-suited for the adjustment of the DRIE processing parameters. The orthogonal experimental design (OED) method, an approach that provides qualitative conclusions, is well suited for recipe tuning, especially for cases where more than two inter-affecting parameters need to be investigated [183].

2.2.1. Recipe Building Using OED Method

The OED method is named for the manner in which parameter settings are selected. With bowing-reduction in mind, the three parameters that have the greatest impact on the formation of bowing defects during DRIE are: the platen power (P_p), the duty cycle of the

platen power (DC_p) and the chamber pressure during the etching sub-steps (p_e). Several initial values are derived for each parameter (e.g., based on experience or literature) in a trial starting etch recipe. The different parameter values (called 'levels' in the OED method) are then used for exploratory experiments in combinations that satisfy the orthogonality condition. To illustrate its relevance to X-ray grating fabrication, representative results from the authors' prior work are included here as examples. Table 2 qualitatively describes the typical effects of different parameters on etching characteristics, e.g., increasing the RF power supply duty cycle increases the etch rate but also decreases the selectivity. It also reports nine etching recipes (1-9) where the three parameters (DC_p, p_e and P_p), each at three levels, are combined in a manner that satisfies the condition of orthogonality. Specifically, and characteristic of an OED recipe table, all possible pairings exist exactly once, e.g., the combination of DC_p=12 % with p_e = 200 W occurs only in recipe 6. By the use of these restricted combinations, the OED method allows evaluation of the impact of a single parameter by virtue of the ability to average out the impact of the others.

Table 2: Example of parameters matrix for the study of RF power supply duty cycle (DC_p), Chamber pressure (p_e), and Platen RF power (P_p) in silicon DRIE with the OED method.

	RF power supply duty cycle (%)	Chamber pressure (mTorr: 0.133 Pa)	Platen RF power (W)
	Etch Rate ↑ Selectivity ↓	Selectivity ↑ Bowing ↓	Selectivity ↓ Bowing ↑
1	12	30	150
2	16	40	150
3	20	50	150
4	20	40	200
5	16	30	200
6	12	50	200
7	12	40	250
8	16	50	250
9	20	30	250

2.2.2. Data Analysis in the OED Method

A series of identical patterned wafers were etched using the parameter combinations listed in Table 2, with the other parameters (e.g., the number of etching/deposition cycles) held constant. Critical dimensions, including the trench opening width, etching depth, sidewall angle, and bottleneck width, were measured and recorded for post-analysis. For the example of minimum linewidth of the silicon lamellae (*c* value in Figures 9a), values for each set of conditions in Table 2 were obtained from the SEM images of the cross sectioned specimens shown in Figure 18. Table 3 provides the post-process data analysis. For the analysis, the *c* values from the three experiments using the same value for a given parameter are first summed. The nine sums obtained from the *c* values, organized according to the process parameter (DC_p, p_e or P_p) in columns and the parameter value in rows (adjacent to the parameter value) are found to the right of *K*. For example, the number 1033.0 nm in the first row below $DC_{p\,(\%)}$ in the row for duty cycle 12 % is the sum of the *c* values measured from tests 1, 6, and 7 (from Table 2) for which the duty cycle of the platen RF power was 12 %. The values in the section K_{avg} immediately beneath is simply the average of the values in the *K* section (i.e., divided by 3). Here, *R* is defined as the range of the average evaluation indices for the different levels of a parameter, i.e., $R = \max(K_{avg}) - \min(K_{avg})$. A larger *R* indicates a stronger influence of that parameter on the evaluated outcome. This definition follows the standard OED analysis procedure [184]. By comparing the measured *c* (Figure 19a), the best value (level) for each parameter can be found, and gratings with higher aspect ratio and better profile control can be produced (Figure 19b).

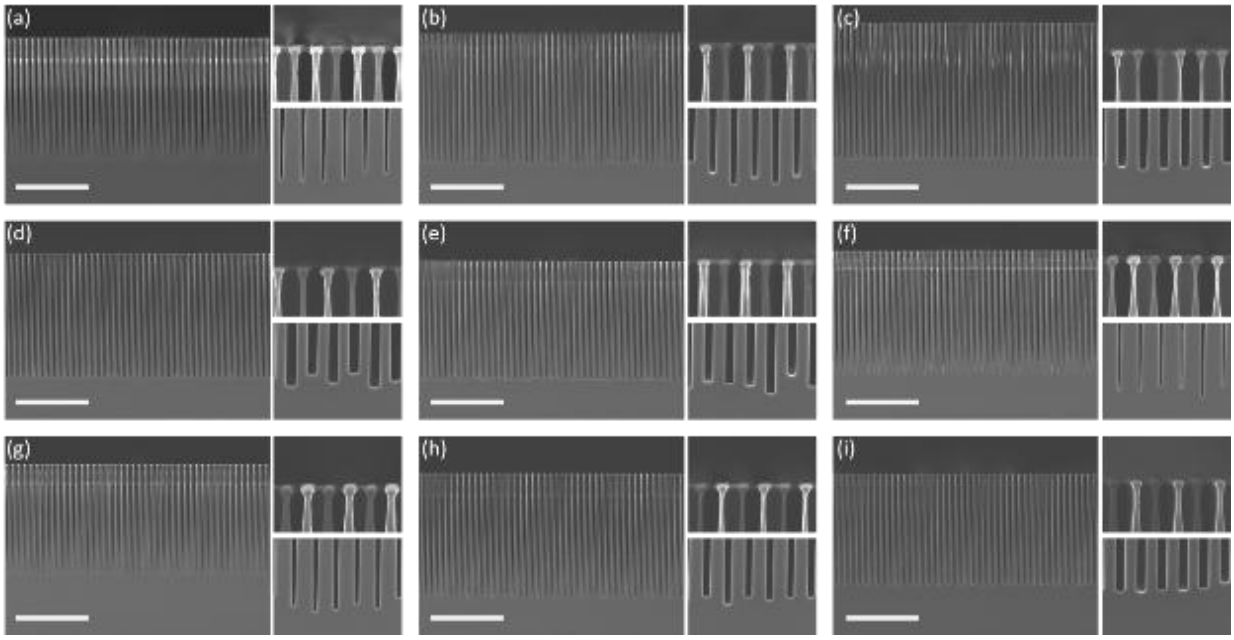

Figure 18: Cross-section SEM images of the gratings from the OED test using (a-i) recipe 1-9. Each set of SEM images includes the overview of the grating (left), close-ups of the top area (top-right) and the bottom area (bottom-right). Reproduced with permission from ref. [1].

Table 3: The *c* value (nm) analysis chart from the OED evaluation

Minimum Linewidth *c* (nm)						
	DC_p (%)	$\sum c_i$	p_e (mTorr)	$\sum c_i$	P_p (W)	$\sum c_i$
K	12	1033.0	30	1153.2	150	768.8
	16	828.9	40	1138.6	200	790.3
	20	838.3	50	408.4	250	1141.1
	DC_p (%)	$\sum c_i/3$	p_e (mTorr)	$\sum c_i/3$	P_p (W)	$\sum c_i/3$
Kavg	12	344.3	30	384.4	150	256.3
	16	276.3	40	379.5	200	263.4
	20	279.4	50	136.1	250	380.4
Least bow	*12%*		*30* mTorr		*250 W*	
R	68.0		248.3		124.1	

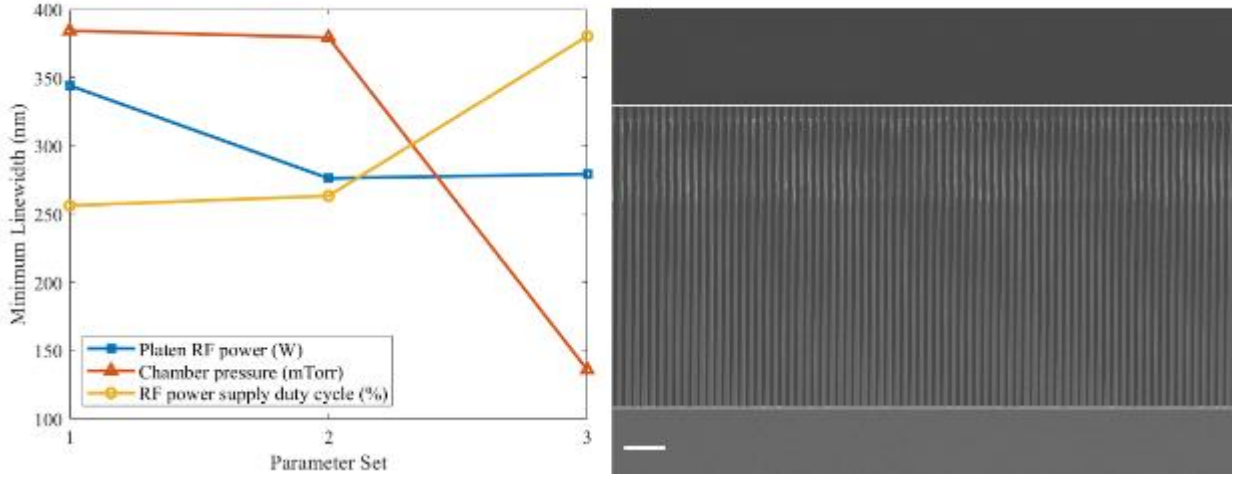

Figure 19: Left: post-process evaluation of the OED experiment results. The curves of the *c* values plotted again the parameter values (each in increasing order) capture the impact of each parameter on bowing in the final etching profile. Right: Cross-section SEM image of a high aspect ratio silicon grating fabricated using a DRIE recipe optimized using the OED method; the scale bar is 20 μm. The grating has a period of 4.2 μm while the etching depth (marked by the two horizontal lines) is 158 μm, resulting in an aspect ratio exceeding 75:1. Reproduced with permission from ref. [1].

3. Metallization

A substantial challenge facing implementation of XGI for imaging applications is the fabrication of absorption gratings [45]. Requirements are especially stringent for X-ray medical diagnostics as a relatively large field of view is necessary. Thus, gratings require microfabrication on area of many squared centimeters [26], with a pitch size in a range of 1 μm to 20 μm and aspect ratio in the range of 10 to 100 that depend on the application energy, specific design and performance requirements. The period or pitch (p_0, p_2) of the absorption (G0, G2) gratings is usually in the range of 1 μm to 20 μm, while the height (h) depends on the X-ray energy and absorption efficiency of the material [185]. High density materials, such as gold [44, 45, 58], iridium [89, 186], platinum [187], palladium [188] and tungsten [80, 189, 190] that provide strong X-ray absorption are deposited in the etched trenches. Transmission through the metal-filled grating lines below 1/e (37 %) or, more typically, below $1/e^2$ (13.7 %) of the original intensity is required. For perspective, a 10 μm thick Au layer can efficiently absorb photons with energies below 20 keV, but for photon energies of 30 keV (60 keV), more than 25 μm (160 μm) of Au is required. Recent work on mammography systems imposed severe design requirements in terms of system length and sensitivity such that small pitch, high aspect ratio G2 gratings were required (p_2 in the range of 1 μm and gold height of 30 μm [58, 191]). The absence of monolithic gratings with sufficiently large field of view necessitates stitching, such as in recent studies of mammography [8] and chest imaging [192], introducing non-trivial solution of positioning and alignment.

Fabrication of metallic X-ray gratings in silicon templates has been demonstrated, with varying degrees of success, using several methodologies: conformal electroplating with partial fill, such as can be used for spatial frequency doubling (vide infra) [45] or (nominally) complete [45, 60, 79] filling. Approaches for the latter include: seedless electroplating through a mask [78, 84]; liquid metal casting of Bi [193] as well as Au and Pb alloys [87, 194]; casting of W particles [80]; atomic layer deposition (ALD) of Ir [89]; bottom-up Au electroplating [59, 61, 195]; and use of the catalyst from metal assisted chemical etching as a seed layer [131, 196]. Each of these techniques has its own benefits and challenges, as detailed in what follows.

3.1. Metal casting

Metal casting approaches seek to adapt the ancient and nominally simple technology to the filling of much smaller features. The cross-sectional SEM images reproduced in Figure 20 showcase typical filling quality. While liquid metal casting [87, 194] is a very promising technique in terms of simplicity of fabrication, it cannot be performed with pure Au (at least in a Si template due to the low melting Au-Si eutectic), while use of lower melting Pb or Bi [193] requires substantial increase of trench height to compensate for the lower attenuation coefficient of these material. A further drawback of the thermally driven process is that metal casting at elevated temperatures results in substantial stressing of the underlying Si wafer due to mismatched thermal expansion coefficients of the Si substrate and cast metal, which can cause failure by fracture. The presence of voids as in casting of W particles (a melt being impractical if not impossible) may limit application in XGI, since the gratings can produce X-ray scattering that complicates dark-field imaging [197].

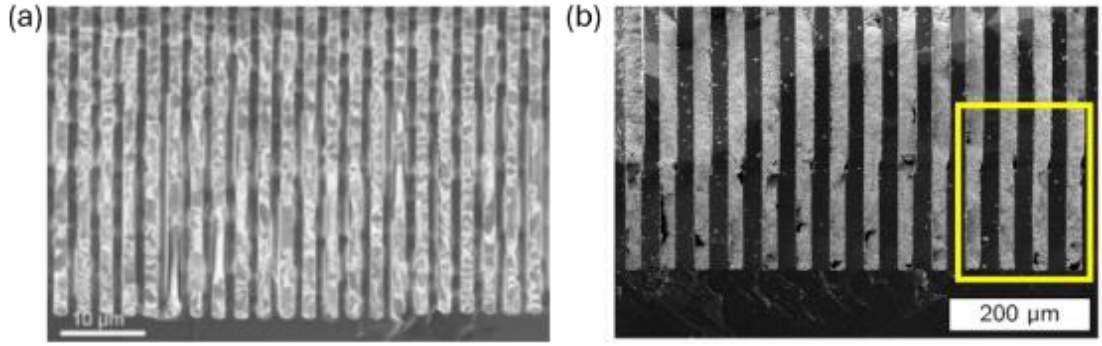

(c)

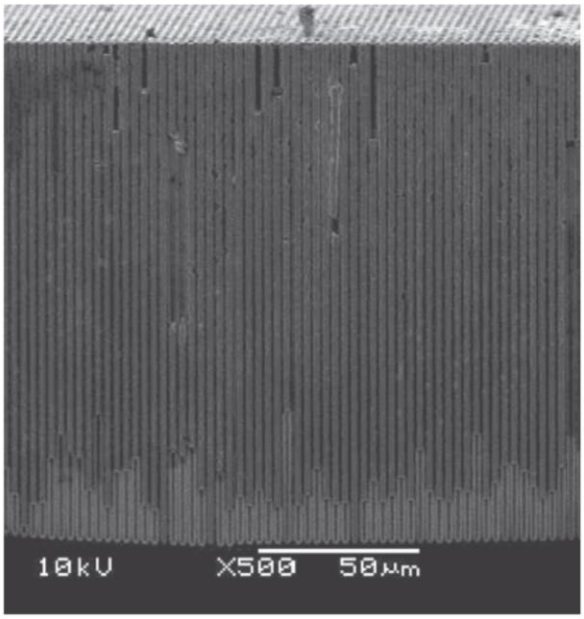

Figure 20: Cross-sectional SEM images of metal filled X-ray gratings representative of different casting methods: (a) metal casting with Au80Sn20 eutectic alloy, reproduced with permission from ref. [194] (b) centrifugal deposition of bimodal tungsten particles, reproduced with permission from ref. [80], (c) Bi casting into 3 μm pitch Si grating with a depth of 150 μm, reproduced with permission from ref. [193].

3.2. Electroplating through a mask

A pre-deposited conducting seed layer is typically required on insulating or dielectric surfaces to serve as an anode for metal electrodeposition. Use of low resistivity Si substrates enables seedless electroplating that utilizes the patterned and etched (Si) wafer itself for through-mask plating [78, 198]. The basic schematic of the process is shown in Figure 21. The etched Si structures are thermally oxidized, then additional oxide layer deposited on top of the structures by PECVD. This additional layer on top allows to open oxide at the bottom of the structures, while keeping the rest of the Si structures electrically isolated. Ohmic contact is deposited at the backside of the wafers. Applying the electric potential to the backside metal layer and using low resistivity wafers allows the electrodeposition of Au to start directly on the surface of the Si trenches and continues upward through the high aspect ratio trenches in the oxidized Si template. This technique was recently used to fabricate structures with aspect ratio up to approximately 25:1 without stabilizing Si bridges (Figure 21) [84]. While it worked well for larger pitches, for a smaller pitch of 1.3 μm and a Au height of 16 μm distortions were observed [84]. The introduction of bridges between the thin Si lamellae can reduce the problem. However, an intrinsic limitation associated with the stresses caused by oxidation of the lamellae prevents use of this technique with smaller

pitches and at higher aspect ratios. The method is also sensitive to sidewall defects that can result in formation of very large Au clusters.

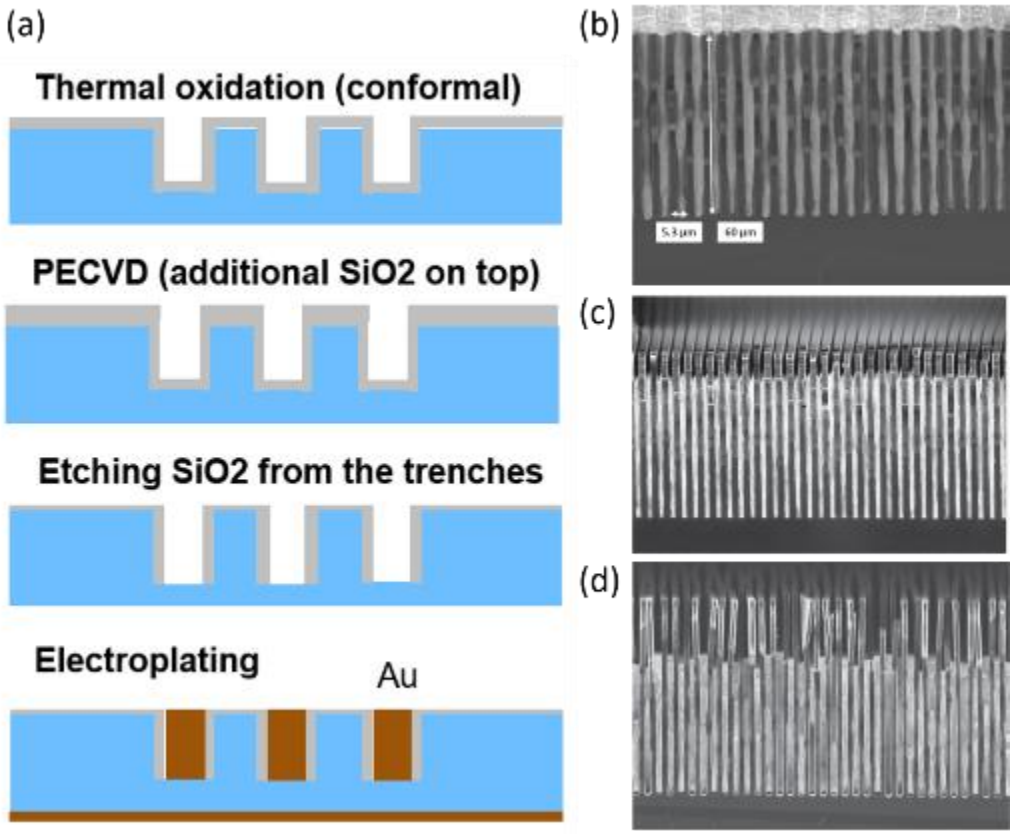

Figure 21. Schematics of fabrication steps (a) and cross-sectional SEM-images of gratings made by seedless electroplating on low resistivity Si wafers through oxidized Si lines: (b) grating pitch 5.3 μm, Au height 60 μm [78], (c) grating pitch 5.4 μm, Au height 69 μm, reproduced with permission from ref. [84], (d) grating pitch 1.3 μm, Au height 16 μm, reproduced with permission from ref. [84].

3.3. Conformal electroplating

ALD of metallic coating has been used to form a metallization layer for subsequent Au electroplating by both conventional damascene approaches [60, 199] and Au bottom-up filling processes [61]. Conformal Au electroplating approaches were demonstrated using ALD deposited Pt [79] and Ru [60] as plating seed layer. Alternatively, seedless conformal Au electroplating was demonstrated on low-resistivity Si wafers patterned with trenches having aspect ratios of up to 45:1 without use of a metal seed layer [58]. Generally, conformal electroplating approaches that are aimed at complete feature filling require slight tapering of the sidewalls, such that the trenches are slightly wider on top as compared to the bottom. This allows electrolyte transport through the trench depth throughout the deposition process, consistent with void-free filling by so-called “geometrical leveling”. However, with higher aspect ratio features, decrease of the trench width during growth progressively

increases the aspect ratio remaining to be filled virtually to infinity. This typically leaves seam-like voids along the center of the metal-filled lines, where the metal layers grown on the opposite sidewalls merge together. Critically, any bottlenecks in the Si trenches become the locations of premature bridging of the deposits from the opposite sidewalls, creating even larger central voids in the metal below the bottleneck.

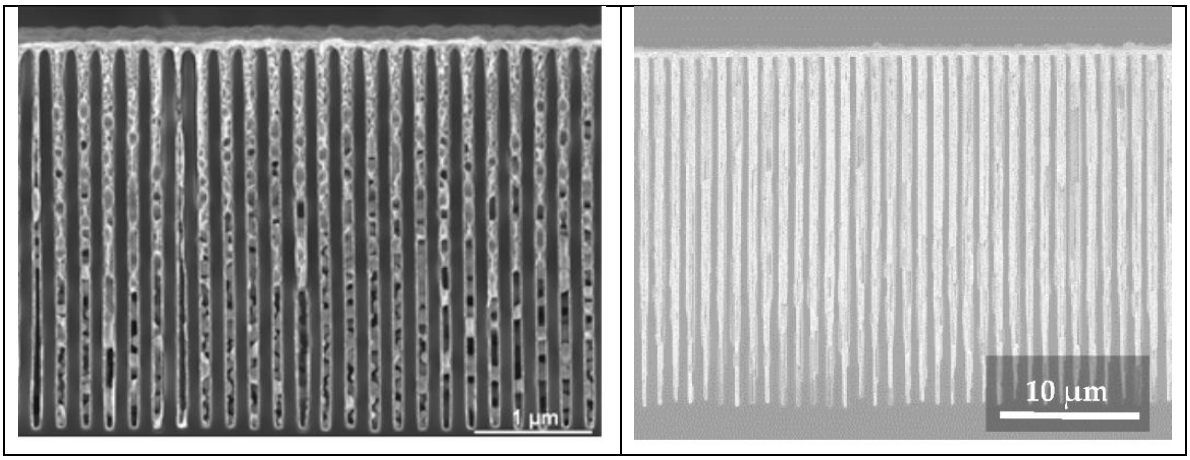

Figure 22. Cross-sectional SEM-images of gratings made by conformal electroplating of high aspect ratio structures in Si: (a) p=400 nm, h≈3.2 μm, AR≈16:1 with voided Au fill by electrodeposition on an ALD deposited Al_2O_3/Pt seed layer, reproduced with permission from ref.[199]; (b) p=1.2 μm, h≈27 μm, AR≈45:1 using back-contact, seedless Au electrodeposition on low-resistivity Si, reproduced with permission from ref. [58].

3.4. Overcoming Aspect Ratio Limits in DRIE with Frequency Doubling

While DRIE is widely used to fabricate high aspect ratio structures, it faces inherent limitations in aspect ratio due to etch constraints, as explained previously. Approaches based on complete metal filling and a 0.5 duty cycle (e.g. the width of the Si lines, at one-half the pitch, equals the trench width), translate the small pitches required for increased sensitivity and thick Au required for use at high X-ray energies into extremely high aspect ratio features in the X-ray absorption gratings. The aspect ratio of the DRIE-fabricated structure for a given pitch can be decreased by a factor of two if the gap between the Si lines is set to be 3× the line width, i.e., using a duty cycle of 0.25 (Si line width / pitch), and the X-ray absorbing metal is deposited conformally until its thickness equals that of the Si lines. The resulting structure has equally spaced high aspect ratio gold lines with alternating Si and air as the low-absorption spacer, as shown in Figure 23a, with the width of the air-filled regions equal to the width of Si. This approach, which effectively doubles the pitch that needs to be implemented by the DRIE, was first demonstrated for fabrication of X-ray gratings by anisotropic KOH wet-etching and Au electroplating [45] (see Figure 23b) and later implemented by DRIE with the absorbing Ir deposited by ALD [200] (see Figure 23c).

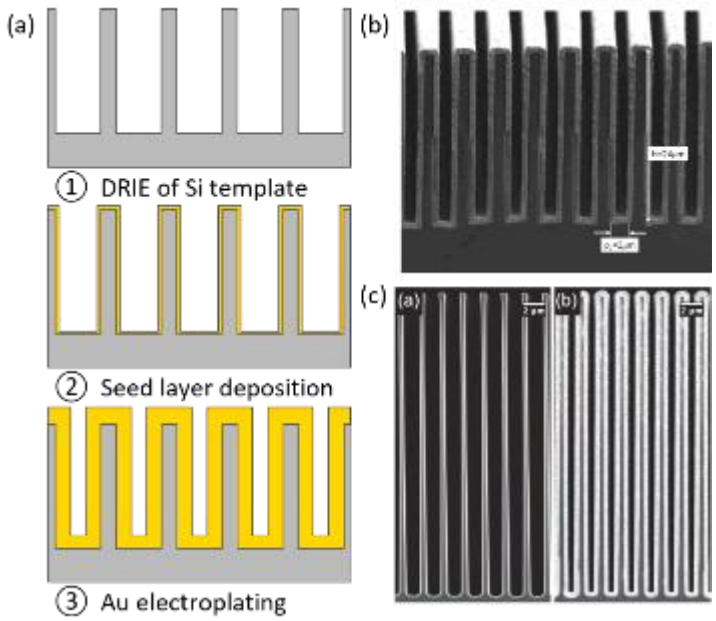

Figure 23: (a) Process flow of the frequency doubling method. (b) Example Au X-ray grating deposited on wet-etched Si template, reproduced with permission from ref. [45]. (c) Example of Si grating (left side) coated by Ir (right side), reproduced with permission from ref. [89].

Increase of the aspect ratio of the final structure through the Au deposition process enables extension of fabrication to pitches beyond the resolution limits of currently available lithographic techniques. Indeed, the Fresnel Zone Plate gratings created using the Ir ALD [200] achieved record resolution. The method, known as spatial frequency multiplication, pitch multiplication, sidewall image transfer, spacer patterning, edge lithography, as well as sidewall assisted double patterning, is also being examined for the development of next generation electronics [201]. That said, this technique requires precise process control of the conformal metal deposition and generally suffers from a decrease of quality with increasing aspect ratio, particularly to create smaller final pitches. Gratings with an aspect ratio of 60:1 have been fabricated by coating Si structures by Ir ALD (Figure 23c [89]) to generate pitch 1 μm absorption grating. While for this particular case, the method was limited to small areas due to a limited supply of precursor in the specific ALD chamber, conformal gold electroplating would not have such a restriction and be more cost-effective option.

3.5. Bottom-up electroplating

Bottom-up Au electrodeposition in the presence of additives is one example of a powerful group of "superconformal" deposition processes that allow void-free filling of complex and high aspect ratio recessed structures embedded in conductive surface without the need for masking. Superconformal filling processes utilize dilute additives to selectively modify the kinetics of metal deposition across the substrate surface, thereby localizing metal

deposition at, or toward, the bottoms of the recessed features to be filled. Such processes underlie the filling of features recessed into metallized dielectric surfaces with copper (i.e., damascene processing) in microelectronics for on-chip and wafer stacking interconnection. Of the two mechanistic variants demonstrated and explained to date [202-204], one relies on surfactant additives whose adsorption on the surface of the growing metal deposit accelerates deposition and which stays on the surface during growth, i.e., a surfactant; critically, its coverage changes with change of the surface area that occurs during growth on non-planar surfaces (the so-called "curvature enhanced accelerator coverage", aka CEAC, mechanism). The other mechanism relies on additives whose adsorption suppresses deposition and which are buried, or otherwise consumed, during deposition.

For void-free gold filling of the high aspect ratio trenches (and vias) most relevant to fabrication of high aspect ratio grating, patented electrolytes and processes utilizing non-toxic sodium-gold sulfite with an accelerating Bi^{3+} ion additive have been shown to be especially efficacious. In particular, with micrometer-per-hour deposition rates at the bottoms of filling features versus nanometer-per hour deposition rates on the sidewalls demonstrated, the technology is capable of void-free filling of features having aspect ratios well in excess of 100:1. Without dwelling on the details, the chemistry utilizes enhanced coverage of the surfactant bismuth additive that occurs as the surface area at the trench bottoms decreases (the CEAC mechanism) as well as a negative correlation of the additive-adsorption kinetics with the metal-ion concentration. The latter, which enhances deposition more strongly at the bottoms of deeper features, is critical to the operation of and, so far, unique to, the gold-filling chemistries [205]. Gratings with pitch of 3 μm and Au height of 85 μm (trench aspect ratio of 56:1) have been filled void-free [59] following pre-deposition of a conformal seed layer of Pt by ALD on the silicon template. The Au deposition rate on the sidewalls is considerably slower than at the bottom, making this method suitable for void-free filling of very high aspect ratio silicon trenches. Among others, it has been used to fabricate 8 cm × 8 cm gratings on 100 mm Si wafers with trenches of 60:1 aspect ratio at 2 μm pitch [206]. It has also been used to Au fill grating templates on 100 mm wafer bent to a uniform 20 cm radius of curvature [207], creating mechanically robust gratings with intrinsic curvatures suitable for application in compact imaging systems. Void-free bottom-up Au fill was also demonstrated during fabrication of gratings with 300 μm and 500 μm deep trenches on 100 mm wafers, suitable for applications at higher X-ray energies [208, 209]; and micrometer [20, 29] and submicrometer [210] pitch gratings suitable for high resolution XGI. Figure 24 shows representative images.

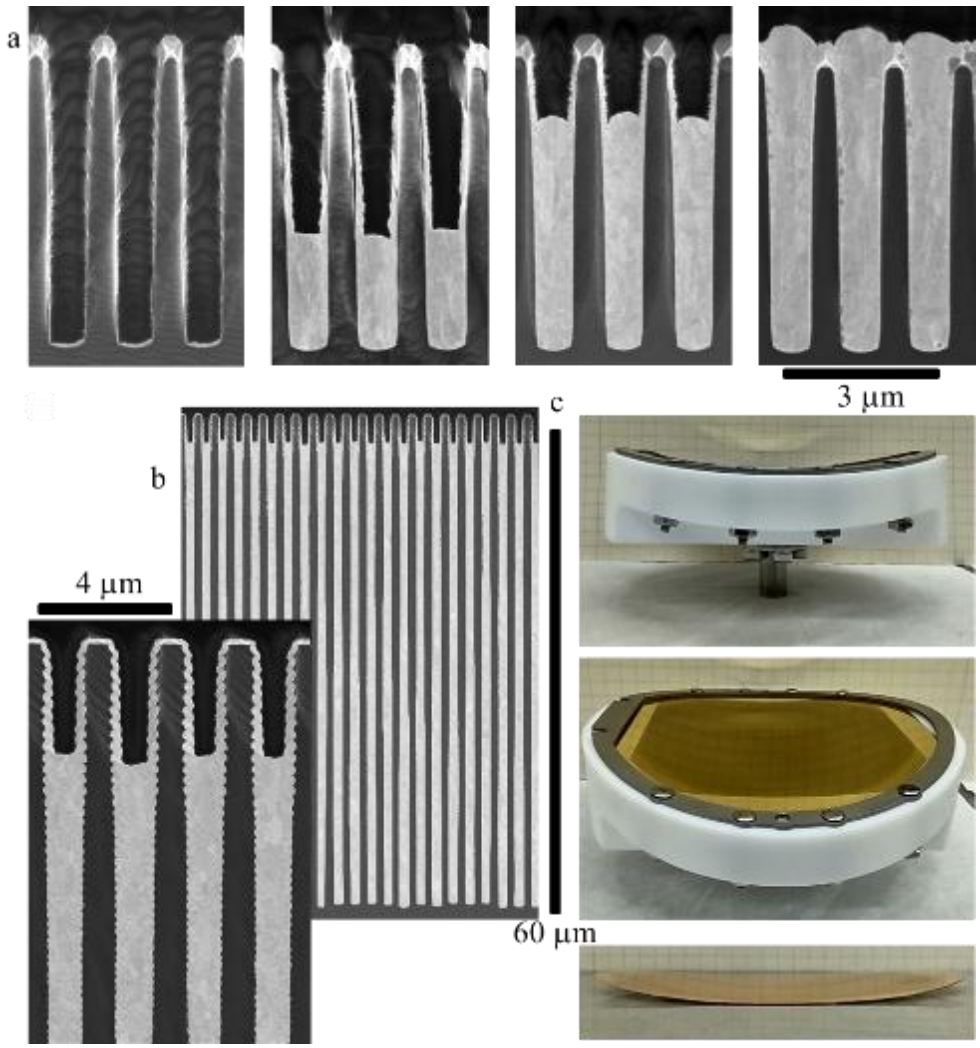

Figure 24: Images of bottom-up Au filling achieved in trenches with fully metallized surfaces by electrodeposition using an additive-based superfilling chemistry. (a) p=1.3 μm, h=5.5 μm gratings with different fractions of bottom-up Au fill. (b) Bottom-up filled p=2 μm, h=60 μm grating. The horizontal profile in the higher magnification image manifests ≈ 60 μm of growth from the bottom surface and less than 0.2 μm of Au deposit on the sidewalls of the fully metallized trenches, reproduced with permission from ref. [206] (c) Photographs of a grating with 100 μm deep trenches at 5.25 μm pitch on 100 mm Si wafer after Au fill while mounted on a holder imposing a 20 cm radius of curvature; the freestanding grating exhibits a ≈ 30 cm retained radius of curvature, reproduced with permission from ref. [207].

3.6. Exemplary application of the bottom-up filled absorption grating

In addition to the reviewed literature, we include here original supporting experiments carried out by the authors to illustrate practical aspects of DRIE-based grating fabrication. These results have not been previously published and are presented solely to complement the review discussion.

The performance of gratings fabricated using the Patterning-Etching-Metallization process flow with bottom-up Au filling is demonstrated in a Talbot-Lau interferometry system consisting of one phase grating and two absorption gratings. The system is a 3 μm-period symmetric design, with the grating patterns prepared using a SUSS MA6 mask aligner. The pattern was transferred from S1805 positive photoresist into a 50 nm Cr hardmask to increase selectivity during the DRIE process. The voltage and current of the X-ray tube source were 40 keV and 1.5 mA, respectively [34]. The 20 keV X-ray design energy of the grating interferometer required a phase grating etched in silicon to a depth of 24 μm, while the absorption gratings were obtained by Au bottom-up filling 30 μm deep etched silicon trenches. The imaging system was arranged to utilize the 11^{th} Talbot order, such that the phase grating (G1) was placed 398 mm away from the X-ray focus point, with the analyzing absorption grating (G2) placed 398 mm downstream of the phase grating for the symmetrical design. The biomedical specimen, a mouse embryo, was placed in front of the phase grating (G1) to lengthen the propagation distance of the beam from the sample to the detector for increased angular sensitivity [11]. Animal maintenance, husbandry and procedures were done in accordance with British Home Office regulations (Animals Scientific Procedures Act 1986). The analyzing grating (G2) was step-scanned over one period of the 3 μm grating pitch at intervals of 0.6 μm, with acquisition times extended to obtain essentially noise-free data at each pixel of the detector for the follow-up image reconstruction. The reconstructed images of the sample are shown in Figure 25. Because imaging by absorption contrast relies on the presence of high Z-elements, such as the calcium and phosphorus found in bones, the phase contrast imaging provides far superior differentiation of the soft tissues of the embryo. The signals provided by absorption versus phase contrast, being responsive to different properties and constituents of the materials in a specimen, are highly complementary.

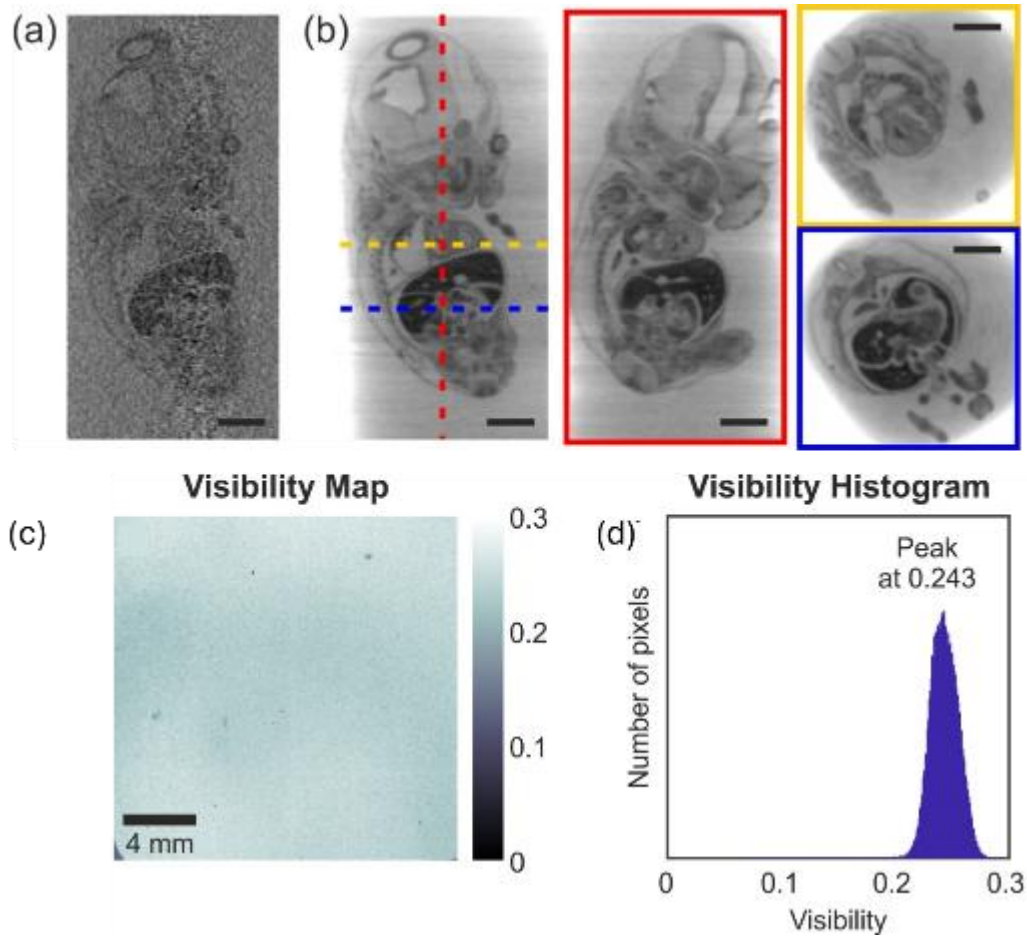

Figure 25: Tomographic reconstruction of a mouse embryo embedded in paraffin wax. (a) The soft tissues of the embryo are barely distinguishable from the background in the absorption contrast image. (b) In the phase contrast images the different tissues of the mouse embryo are clearly distinguished. Tomographic slices along the dashed lines in the left-most image are shown in the correspondingly outlined images. All scale bars are 1 mm. (c) Visibility map and (d) visibility histogram of the X-ray imaging system used to acquire the phase contrast images. Illustrative results obtained by the authors.

4. Future Challenges and Perspectives

DRIE processes are, and will remain for the foreseeable future, the dominant industrial technology for fabrication of high aspect ratio microstructures [211]. Achieving precise control over etching profiles while pushing the limits of aspect ratio is the main challenge for X-ray optics micro-fabrication. Thanks to developments in both process and hardware for DRIE technology, as well as its flexibility and robustness, the Patterning–Etching–Metallization process flow has become increasingly popular within the subspecialty of X-ray transmission gratings for phase-contrast imaging. As noted, plasma etching also permits

tilted etching [179] that enables the production of gratings with exotic designs, such as fan-shaped grating [180] to conform to the divergence of X-ray beams from conventional tube sources [207]. Full utilization of X-ray phase contrast imaging technology will require gratings of much higher quality, bringing new challenges to the DRIE processing [197, 212]. From the process side, the cost and inefficiency of conventional recipe-tuning protocols is prompting the rise of computer-aided recipe-tuning [139, 213, 214]; machine learning (ML) may further accelerate this shift [215-218]. The complexity of the plasma environment and changes of the etching chamber conditions are such that numerous parameters need to be taken into account, making even the OED approach intrinsically limited. One may hope that the rise of advanced ML-based models taught by experiment will improve the situation [219]. From the hardware side, ICP systems equipped with fast-switching mass flow controllers remain the workhorses for the fabrication of high aspect ratio microstructures in X-ray gratings. Cryogenic-compatible ICP etching systems could enable fabrication of higher aspect ratio features, especially for sub-micron applications [158, 220]. Although not suitable for the fabrication of gratings that have relatively large periods, efforts to use smaller period gratings for increased resolution in XGI systems could make cryogenic etching useful for manufacture of X-ray gratings. DRIE-based Patterning-Etching-Metallization can be considered a robust means of fabricating high-quality X-ray optics with aspect ratios reaching more than 70:1, and approaches for spatial frequency multiplication could boost this value by (at least) a factor of 3. In the end, simplified process tuning and reproducible fabrication of high-quality gratings will push XGI from localized academic exercise towards broadscale commercial application.

Author Contributions: All authors contributed equally to this manuscript. All authors have read and agreed to the published version of the manuscript.

Funding: This work was supported by GratXray AG; European Research
Council [310005]; Schweizerischer Nationalfonds zur Förderung der Wissenschaftlichen Forschung [159263, 206021-177036, 206021-189662, CRSII2 154472, CRSII5 183568]; lottery fund SwissLOS of the Kanton of Aargau; NanoArgovia Grant (Swiss Nanoscience Institute) [13.01 ”NANOCREATE”] ; PHRT-TT [2022-572 “INTIMACY”].

Acknowledgments: The authors would like to thank Dr. Vitaliy Guzenko (PSI), and Dr. Craig Lawley (PSI), for the relevant experimental validation works. We thank Andrew C. Cook for kindly providing the mouse embryo sample used in this study.

Conflicts of Interest: *M. Stampanoni is a member of the BoD and a co-founder of GratXray AG.*

References

[1] Z. Shi, Microfabrication of X-ray gratings: towards non conventional profile control in high aspect ratio structures, ETH Zurich, 2022.
[2] A. Momose, S. Kawamoto, I. Koyama, Y. Hamaishi, K. Takai, Y. Suzuki, Demonstration of X-Ray Talbot Interferometry, Japanese Journal of Applied Physics 42(Part 2, No. 7B) (2003) L866-L868.
[3] F. Pfeiffer, T. Weitkamp, O. Bunk, C. David, Phase retrieval and differential phase-contrast imaging with low-brilliance X-ray sources, Nature Physics 2(4) (2006) 258-261.
[4] F. Pfeiffer, M. Bech, O. Bunk, P. Kraft, E.F. Eikenberry, C. Brönnimann, C. Grünzweig, C. David, Hard-X-ray dark-field imaging using a grating interferometer, Nature Materials 7(2) (2008) 134-137.
[5] A. Momose, W. Yashiro, K. Kido, J. Kiyohara, C. Makifuchi, T. Ito, S. Nagatsuka, C. Honda, D. Noda, T. Hattori, T. Endo, M. Nagashima, J. Tanaka, X-ray phase imaging: from synchrotron to hospital, Philosophical Transactions of the Royal Society A: Mathematical, Physical and Engineering Sciences 372(2010) (2014) 20130023.
[6] K. Willer, A.A. Fingerle, L.B. Gromann, F. De Marco, J. Herzen, K. Achterhold, B. Gleich, D. Muenzel, K. Scherer, M. Renz, B. Renger, F. Kopp, F. Kriner, F. Fischer, C. Braun, S. Auweter, K. Hellbach, M.F. Reiser, T. Schroeter, J. Mohr, A. Yaroshenko, H.-I. Maack, T. Pralow, H. van der Heijden, R. Proksa, T. Koehler, N. Wieberneit, K. Rindt, E.J. Rummeny, F. Pfeiffer, P.B. Noël, X-ray dark-field imaging of the human lung—A feasibility study on a deceased body, PLOS ONE 13(9) (2018) e0204565.
[7] M. Stampanoni, Z. Wang, T. Thüring, C. David, E. Roessl, M. Trippel, R.A. Kubik-Huch, G. Singer, M.K. Hohl, N. Hauser, The First Analysis and Clinical Evaluation of Native Breast Tissue Using Differential Phase-Contrast Mammography, Investigative Radiology 46(12) (2011).
[8] C. Arboleda, Z. Wang, K. Jefimovs, T. Koehler, U. Van Stevendaal, N. Kuhn, B. David, S. Prevrhal, K. Lång, S. Forte, R.A. Kubik-Huch, C. Leo, G. Singer, M. Marcon, A. Boss, E. Roessl, M. Stampanoni, Towards clinical grating-interferometry mammography, European Radiology 30(3) (2020) 1419-1425.
[9] M. Kagias, Z. Wang, M.E. Birkbak, E. Lauridsen, M. Abis, G. Lovric, K. Jefimovs, M. Stampanoni, Diffractive small angle X-ray scattering imaging for anisotropic structures, Nature Communications 10(1) (2019) 5130.
[10] G. Zentai, X-ray imaging for homeland security, International Journal of Signal and Imaging Systems Engineering 3(1) (2010) 13-20.
[11] J. Vila-Comamala, L. Romano, K. Jefimovs, H. Dejea, A. Bonnin, A.C. Cook, I. Planinc, M. Cikes, Z. Wang, M. Stampanoni, High sensitivity X-ray phase contrast imaging by laboratory grating-based interferometry at high Talbot order geometry, Opt. Express 29(2) (2021) 2049-2064.
[12] F.J. Koch, C. Detlefs, T.J. Schröter, D. Kunka, A. Last, J. Mohr, Quantitative characterization of X-ray lenses from two fabrication techniques with grating interferometry, Opt. Express 24(9) (2016) 9168-9177.
[13] P. Simon, B. Thomas, V. Manuel, M. Pascal, G. Alex, A. Jana, G. Nikolai, H. Julia, S. Joachim, P. Franz, Fabrication of x-ray absorption gratings via deep x-ray lithography using a

conventional x-ray tube, Journal of Micro/Nanopatterning, Materials, and Metrology 20(4) (2021) 043801.
[14] A. Pereira, S. Spindler, Z. Shi, L. Romano, M. Rawlik, F. Marone, D. Josell, M. Stauber, M. Stampanoni, Quantifying grating defects in X-ray Talbot-Lau interferometry through a comparative study of two fabrication techniques, Scientific Reports 15(1) (2025) 14223.
[15] Z. Shi, K. Jefimovs, L. Romano, M. Stampanoni, Optimization of displacement Talbot lithography for fabrication of uniform high aspect ratio gratings, Japanese Journal of Applied Physics 60(SC) (2021) SCCA01.
[16] D.L. Voronov, E.M. Gullikson, H.A. Padmore, Large area nanoimprint enables ultra-precise x-ray diffraction gratings, Opt. Express 25(19) (2017) 23334-23342.
[17] C.T. DeRoo, J. Termini, F. Grisé, R.L. McEntaffer, B.D. Donovan, C. Eichfeld, Limiting Spectral Resolution of a Reflection Grating Made via Electron-beam Lithography, The Astrophysical Journal 904(2) (2020) 142.
[18] S. Mudide, N. Keller, G. Andrew Antonelli, G. Cruz, J. Hart, A.R. Bruccoleri, R.K. Heilmann, M.L. Schattenburg, Machine learning driven measurement of high-aspect-ratio nanostructures using Mueller matrix spectroscopic ellipsometry, Journal of Vacuum Science & Technology B 43(1) (2025) 012801.
[19] C. Rauch, S. Schreiner, P. Meyer, V. Ludwig, M. Schneider, C. Sowinski, G. Anton, T. Michel, S. Funk, Enhanced grating characterization method for absorbing x-ray gratings by bidirectional angular x-ray transmission, Measurement Science and Technology 36(6) (2025) 065413.
[20] S. Spindler, A. Pereira, P. Sommer, M. Rawlik, L. Romano, M. Stampanoni, Simulation framework for X-ray grating interferometry optimization, Optics Express 33(1) (2025) 1345-1358.
[21] C. Organista, M. Kagias, R. Tang, Z. Shi, K. Jefimovs, M.N. Boone, M. Stampanoni, Optimization of the visibility of a tunable dual-phase x-ray grating interferometer, Opt. Continuum 2(1) (2023) 232-248.
[22] V. Revol, C. Kottler, R. Kaufmann, U. Straumann, C. Urban, Noise analysis of grating-based x-ray differential phase contrast imaging, Review of Scientific Instruments 81(7) (2010).
[23] A. Momose, X-ray phase imaging reaching clinical uses, Physica Medica 79 (2020) 93-102.
[24] L. Quenot, S. Bohic, E. Brun, X-ray Phase Contrast Imaging from Synchrotron to Conventional Sources: A Review of the Existing Techniques for Biological Applications, Applied Sciences, 2022.
[25] Z. Wang, Recent advances in X-ray grating-based dark-field imaging, TrAC Trends in Analytical Chemistry 181 (2024) 118052.
[26] T. Weitkamp, A. Diaz, C. David, F. Pfeiffer, M. Stampanoni, P. Cloetens, E. Ziegler, X-ray phase imaging with a grating interferometer, Opt. Express 13(16) (2005) 6296-6304.
[27] M. Kagias, Z. Wang, K. Jefimovs, M. Stampanoni, Dual phase grating interferometer for tunable dark-field sensitivity, Applied Physics Letters 110(1) (2017) 014105.

[28] R. Tang, C. Organista, L. Romano, L. Van Hoorebeke, M. Stampanoni, J. Aelterman, M.N. Boone, Pixel-wise beam-hardening correction for dark-field signal in X-ray dual-phase grating interferometry, Opt Express 31(24) (2023) 40450-40468.
[29] C. Organista, R. Tang, Z. Shi, K. Jefimovs, D. Josell, L. Romano, S. Spindler, P. Kibleur, B. Blykers, M. Stampanoni, M.N. Boone, Implementation of a dual-phase grating interferometer for multi-scale characterization of building materials by tunable dark-field imaging, Sci Rep 14(1) (2024) 384.
[30] I. Snigireva, P. Maxim, A. and Snigirev, Diamond X-Ray Refractive Optics, Synchrotron Radiation News 34(6) (2021) 12-20.
[31] D. Cocco, G. Cutler, M. Sanchez del Rio, L. Rebuffi, X. Shi, K. Yamauchi, Wavefront preserving X-ray optics for Synchrotron and Free Electron Laser photon beam transport systems, Physics Reports 974 (2022) 1-40.
[32] K. Li, Y. Liu, M. Seaberg, M. Chollet, T.M. Weiss, A. Sakdinawat, Wavefront preserving and high efficiency diamond grating beam splitter for x-ray free electron laser, Opt. Express 28(8) (2020) 10939-10950.
[33] M. Makita, P. Karvinen, V.A. Guzenko, N. Kujala, P. Vagovic, C. David, Fabrication of diamond diffraction gratings for experiments with intense hard x-rays, Microelectronic Engineering 176 (2017) 75-78.
[34] M. Polikarpov, J. Vila-Comamala, Z. Wang, A. Pereira, S. van Gogh, C. Gasser, K. Jefimovs, L. Romano, Z. Varga, K. Lang, M. Schmeltz, S. Tessarini, M. Rawlik, E. Jermann, S. Lewis, W. Yun, M. Stampanoni, Towards virtual histology with X-ray grating interferometry, Sci Rep 13(1) (2023) 9049.
[35] N. Marchack, L. Buzi, D.B. Farmer, H. Miyazoe, J.M. Papalia, H. Yan, G. Totir, S.U. Engelmann, Plasma processing for advanced microelectronics beyond CMOS, Journal of Applied Physics 130(8) (2021) 080901.
[36] M. Zahedinejad, S.D. Farimani, M. Khaje, H. Mehrara, A. Erfanian, F. Zeinali, Deep and vertical silicon bulk micromachining using metal assisted chemical etching, Journal of Micromechanics and Microengineering 23(5) (2013) 055015.
[37] B. Hamelin, L. Li, A. Daruwalla, C.P. Wong, F. Ayazi, High-aspect-ratio sub-micron trench etching on SOI using wet metal-assisted chemical etching (MaCE) process, 2016 IEEE 29th International Conference on Micro Electro Mechanical Systems (MEMS), 2016, pp. 447-450.
[38] Y. Wan, Z. Qiu, Y. Hong, Y. Wang, J. Zhang, Q. Liu, Z. Wu, C.F. Guo, A Highly Sensitive Flexible Capacitive Tactile Sensor with Sparse and High-Aspect-Ratio Microstructures, Advanced Electronic Materials 4(4) (2018) 1700586.
[39] G.J. Snyder, J.R. Lim, C.-K. Huang, J.-P. Fleurial, Thermoelectric microdevice fabricated by a MEMS-like electrochemical process, Nature Materials 2(8) (2003) 528-531.
[40] M.R. Zamfir, H.T. Nguyen, E. Moyen, Y.H. Lee, D. Pribat, Silicon nanowires for Li-based battery anodes: a review, Journal of Materials Chemistry A 1(34) (2013) 9566-9586.
[41] E. Garnett, P. Yang, Light Trapping in Silicon Nanowire Solar Cells, Nano Letters 10(3) (2010) 1082-1087.
[42] K. Balasundaram, P.K. Mohseni, Y.-C. Shuai, D. Zhao, W. Zhou, X. Li, Photonic crystal membrane reflectors by magnetic field-guided metal-assisted chemical etching, Applied Physics Letters 103(21) (2013) 214103.

[43] D. Noda, M. Tanaka, K. Shimada, W. Yashiro, A. Momose, T. Hattori, Fabrication of large area diffraction grating using LIGA process, Microsystem Technologies 14(9) (2008) 1311-1315.
[44] J. Mohr, T. Grund, D. Kunka, J. Kenntner, J. Leuthold, J. Meiser, J. Schulz, M. Walter, High aspect ratio gratings for X-ray phase contrast imaging, AIP Conference Proceedings 1466(1) (2012) 41-50.
[45] C. David, J. Bruder, T. Rohbeck, C. Grünzweig, C. Kottler, A. Diaz, O. Bunk, F. Pfeiffer, Fabrication of diffraction gratings for hard X-ray phase contrast imaging, Microelectronic Engineering 84(5) (2007) 1172-1177.
[46] J. Kenntner, V. Altapova, T. Grund, F.J. Pantenburg, J. Meiser, T. Baumbach, J. Mohr, Fabrication and characterization of analyzer gratings with high aspect ratios for phase contrast imaging using a Talbot interferometer, AIP Conference Proceedings 1437(1) (2012) 89-93.
[47] F. Abrar, B. Thomas, M. Jürgen, M. Pascal, Influence of secondary effects in the fabrication of submicron resist structures using deep x-ray lithography, Journal of Micro/Nanolithography, MEMS, and MOEMS 18(2) (2019) 023502.
[48] K. Ishikawa, K. Karahashi, T. Ishijima, S.I. Cho, S. Elliott, D. Hausmann, D. Mocuta, A. Wilson, K. Kinoshita, Progress in nanoscale dry processes for fabrication of high-aspect-ratio features: How can we control critical dimension uniformity at the bottom?, Japanese Journal of Applied Physics 57(6S2) (2018) 06JA01.
[49] P.S. Finnegan, A.E. Hollowell, C.L. Arrington, A.L. Dagel, High aspect ratio anisotropic silicon etching for x-ray phase contrast imaging grating fabrication, Materials Science in Semiconductor Processing 92 (2019) 80-85.
[50] A.E. Hollowell, C.L. Arrington, P. Finnegan, K. Musick, P. Resnick, S. Volk, A.L. Dagel, Double sided grating fabrication for high energy X-ray phase contrast imaging, Materials Science in Semiconductor Processing 92 (2019) 86-90.
[51] L. Romano, M. Kagias, J. Vila-Comamala, K. Jefimovs, L.-T. Tseng, V.A. Guzenko, M. Stampanoni, Metal assisted chemical etching of silicon in the gas phase: a nanofabrication platform for X-ray optics, Nanoscale Horizons 5(5) (2020) 869-879.
[52] Y. Shimizu, Laser Interference Lithography for Fabrication of Planar Scale Gratings for Optical Metrology, Nanomanufacturing and Metrology 4(1) (2021) 3-27.
[53] K. Jefimovs, L. Romano, J. Vila-Comamala, M. Kagias, Z. Wang, L. Wang, C. Dais, H. Solak, M. Stampanoni, High-aspect ratio silicon structures by displacement Talbot lithography and Bosch etching, Proc.SPIE, 2017.
[54] L. Li, B. Li, C. Zhang, C.-C. Tuan, Z. Lin, C.-P. Wong, A facile and low-cost route to high-aspect-ratio microstructures on silicon via a judicious combination of flow-enabled self-assembly and metal-assisted chemical etching, Journal of Materials Chemistry C 4(38) (2016) 8953-8961.
[55] W. Yashiro, D. Noda, T. Hattori, K. Hayashi, A. Momose, H. Kato, A metallic glass grating for X-ray grating interferometers fabricated by imprinting, Applied Physics Express 7(3) (2014) 032501.

[56] W. Yashiro, K. Kato, M. Sadeghilaridjani, A. Momose, T. Shinohara, H. Kato, X-ray phase imaging using a Gd-based absorption grating fabricated by imprinting technique, Japanese Journal of Applied Physics 55(4) (2016) 048003.
[57] Z. Shi, K. Jefimovs, L. Romano, M. Stampanoni, Towards the Fabrication of High-Aspect-Ratio Silicon Gratings by Deep Reactive Ion Etching, Micromachines 11(9) (2020) 864.
[58] K. Jefimovs, J. Vila-Comamala, C. Arboleda, Z. Wang, L. Romano, Z. Shi, M. Kagias, M. Stampanoni, Fabrication of X-ray Gratings for Interferometric Imaging by Conformal Seedless Gold Electroplating, Micromachines 12(5) (2021) 517.
[59] D. Josell, Z. Shi, K. Jefimovs, L. Romano, J. Vila-Comamala, T.P. Moffat, Pushing the Limits of Bottom-Up Gold Filling for X-ray Grating Interferometry, Journal of The Electrochemical Society 167(13) (2020) 132504.
[60] T.-E. Song, S. Lee, H. Han, S. Jung, S.-H. Kim, M.J. Kim, S.W. Lee, C.W.J.J.o.V.S. Ahn, S. Technology A: Vacuum, Films, Evaluation of grating realized via pulse current electroplating combined with atomic layer deposition as an x-ray grating interferometer, 37(3) (2019) 030903.
[61] D. Josell, S. Ambrozik, M.E. Williams, A.E. Hollowell, C. Arrington, S. Muramoto, T.P. Moffat, Exploring the Limits of Bottom-Up Gold Filling to Fabricate Diffraction Gratings, Journal of The Electrochemical Society 166(16) (2019) D898.
[62] R.K. Heilmann, D.P. Huenemoerder, J.A. McCoy, R.L. McEntaffer, Diffraction Gratings for X-ray Spectroscopy, arXiv [astro-ph.IM] (2024).
[63] A.R. Bruccoleri, R.K. Heilmann, M.L. Schattenburg, Fabrication process for 200 nm-pitch polished freestanding ultrahigh aspect ratio gratings, Journal of Vacuum Science & Technology B 34(6) (2016) 06KD02.
[64] R.K. Heilmann, A.R. Bruccoleri, V. Burwitz, C. DeRoo, A. Garner, H.M. Günther, E.M. Gullikson, G. Hartner, E. Hertz, A. Langmeier, T. Müller, S. Rukdee, T. Schmidt, R.K. Smith, M.L. Schattenburg, X-Ray Performance of Critical-angle Transmission Grating Prototypes for the Arcus Mission, The Astrophysical Journal 934(2) (2022) 171.
[65] F. Siewert, B. Lochel, J. Buchheim, F. Eggenstein, A. Firsov, G. Gwalt, O. Kutz, S. Lemke, B. Nelles, I. Rudolph, F. Schafers, T. Seliger, F. Senf, A. Sokolov, C. Waberski, J. Wolf, T. Zeschke, I. Zizak, R. Follath, T. Arnold, F. Frost, F. Pietag, A. Erko, Gratings for synchrotron and FEL beamlines: a project for the manufacture of ultra-precise gratings at Helmholtz Zentrum Berlin, Journal of Synchrotron Radiation 25(1) (2018) 91-99.
[66] A.E. Franke, M.L. Schattenburg, E.M. Gullikson, J. Cottam, S.M. Kahn, A. Rasmussen, Super-smooth x-ray reflection grating fabrication, Journal of Vacuum Science & Technology B: Microelectronics and Nanometer Structures Processing, Measurement, and Phenomena 15(6) (1997) 2940-2945.
[67] D.M. Miles, R. McCurdy, M. Labella, R.L. McEntaffer, F. Grisé, J. McCoy, J.H. Tutt, Reflection grating fabrication for the Rockets for Extended-source X-ray Spectroscopy, Experimental Astronomy 59(3) (2025) 41.
[68] C.T. DeRoo, R.L. McEntaffer, B.D. Donovan, F. Grisé, C. Eichfeld, V. Burwitz, G. Hartner, C. Pelliciari, M.-M. La Caria, Large-format X-Ray Reflection Grating Operated in an Echelle-like Mounting, The Astrophysical Journal 897(1) (2020) 92.

[69] C. David, V. Guzenko, Fabrication of blazed diffractive optics by through-mask oxidation, (2025).
[70] C. Grünzweig, F. Pfeiffer, O. Bunk, T. Donath, G. Kühne, G. Frei, M. Dierolf, C. David, Design, fabrication, and characterization of diffraction gratings for neutron phase contrast imaging, Review of Scientific Instruments 79(5) (2008) 053703.
[71] A. Momose, H. Takano, Y. Wu, K. Hashimoto, T. Samoto, M. Hoshino, Y. Seki, T. Shinohara, Recent Progress in X-ray and Neutron Phase Imaging with Gratings, Quantum Beam Science, 2020.
[72] J. Valsecchi, M. Strobl, R.P. Harti, C. Carminati, P. Trtik, A. Kaestner, C. Grünzweig, Z. Wang, K. Jefimovs, M. Kagias, Characterization of oriented microstructures through anisotropic small-angle scattering by 2D neutron dark-field imaging, Communications Physics 3(1) (2020) 42.
[73] I. Hidrovo, J. Dey, H. Meyer, D.S. Hussey, N.N. Klimov, L.G. Butler, K. Ham, W. Newhauser, Neutron interferometry using a single modulated phase grating, Review of Scientific Instruments 94(4) (2023) 045110.
[74] J. Kim, S.W. Lee, G. Cho, Visibility evaluation of a neutron grating interferometer operated with a polychromatic thermal neutron beam, Nuclear Instruments and Methods in Physics Research Section A: Accelerators, Spectrometers, Detectors and Associated Equipment 746 (2014) 26-32.
[75] M. Sadeghilaridjani, K. Kato, T. Shinohara, W. Yashiro, A. Momose, H. Kato, High aspect ratio grating by isochronal imprinting of less viscous workable Gd-based metallic glass for neutron phase imaging, Intermetallics 78 (2016) 55-63.
[76] Y. Seki, T. Shinohara, J.D. Parker, W. Yashiro, A. Momose, K. Kato, H. Kato, M. Sadeghilaridjani, Y. Otake, Y. Kiyanagi, Development of Multi-colored Neutron Talbot–Lau Interferometer with Absorption Grating Fabricated by Imprinting Method of Metallic Glass, Journal of the Physical Society of Japan 86(4) (2017) 044001.
[77] M. Busi, J. Shen, M. Bacak, M.C. Zdora, J. Čapek, J. Valsecchi, M. Strobl, Multi-directional neutron dark-field imaging with single absorption grating, Scientific Reports 13(1) (2023) 15274.
[78] D. Noda, A. Tokuoka, T. Hattori, Fabrication of high aspect ratio X-ray grating using silicon dry etching method, AIP Conference Proceedings 1466(1) (2012) 187-192.
[79] H. Miao, A.A. Gomella, N. Chedid, L. Chen, H. Wen, Fabrication of 200 nm Period Hard X-ray Phase Gratings, Nano Letters 14(6) (2014) 3453-3458.
[80] S. Pinzek, A. Gustschin, N. Gustschin, M. Viermetz, F. Pfeiffer, Fabrication of X-ray absorption gratings by centrifugal deposition of bimodal tungsten particles in high aspect ratio silicon templates, Scientific Reports 12(1) (2022) 5405.
[81] G. Hurvitz, Y. Ehrlich, G. Strum, Z. Shpilman, I. Levy, M. Fraenkel, Advanced experimental applications for x-ray transmission gratings spectroscopy using a novel grating fabrication method, Review of Scientific Instruments 83(8) (2012) 083109.
[82] C.M. Silvestre, J.H. Hemmingsen, E.S. Dreier, J. Kehres, O. Hansen, Laser ablation of high-aspect-ratio hole arrays in tungsten for X-ray applications, Microelectronic Engineering 209 (2019) 60-65.

[83] D.L. Voronov, P. Lum, P. Naulleau, E.M. Gullikson, A.V. Fedorov, H.A. Padmore, X-ray diffraction gratings: Precise control of ultra-low blaze angle via anisotropic wet etching, Applied Physics Letters 109(4) (2016) 043112.
[84] M. Kagias, Z. Wang, V.A. Guzenko, C. David, M. Stampanoni, K. Jefimovs, Fabrication of Au gratings by seedless electroplating for X-ray grating interferometry, Materials Science in Semiconductor Processing 92 (2019) 73-79.
[85] M. Matsumoto, K. Takiguchi, M. Tanaka, Y. Hunabiki, H. Takeda, A. Momose, Y. Utsumi, T. Hattori, Fabrication of diffraction grating for X-ray Talbot interferometer, Microsystem Technologies 13(5) (2007) 543-546.
[86] D. Josell, Z. Shi, K. Jefimovs, V.A. Guzenko, C. Beauchamp, L. Peer, M. Polikarpov, T.P. Moffat, Bottom-Up Gold Filling in New Geometries and Yet Higher Aspect Ratio Gratings for Hard X-ray Interferometry, Journal of The Electrochemical Society 168(8) (2021) 082508.
[87] L. Romano, J. Vila-Comamala, M. Kagias, K. Vogelsang, H. Schift, M. Stampanoni, K. Jefimovs, High aspect ratio metal microcasting by hot embossing for X-ray optics fabrication, Microelectronic Engineering 176 (2017) 6-10.
[88] Y. Lei, Y. Du, J. Li, Z. Zhao, X. Liu, J. Guo, H. Niu, Fabrication of x-ray absorption gratings via micro-casting for grating-based phase contrast imaging, Journal of Micromechanics and Microengineering 24(1) (2014) 015007.
[89] J. Vila-Comamala, L. Romano, V. Guzenko, M. Kagias, M. Stampanoni, K. Jefimovs, Towards sub-micrometer high aspect ratio X-ray gratings by atomic layer deposition of iridium, Microelectronic Engineering 192 (2018) 19-24.
[90] D. Hojo, C. Kamezawa, K. Hyodo, W. Yashiro, Fabrication of X-ray absorption grating using an ultracentrifuge machine, Japanese Journal of Applied Physics 58(8) (2019) 088003.
[91] M.H. Lim, T.E. Murphy, J. Ferrera, J.N. Damask, H.I. Smith, Fabrication techniques for grating-based optical devices, Journal of Vacuum Science & Technology B: Microelectronics and Nanometer Structures Processing, Measurement, and Phenomena 17(6) (1999) 3208-3211.
[92] S. Gorelick, J. Vila-Comamala, V. Guzenko, R. Mokso, M. Stampanoni, C. David, Direct e-beam writing of high aspect ratio nanostructures in PMMA: A tool for diffractive X-ray optics fabrication, Microelectronic Engineering 87(5) (2010) 1052-1056.
[93] C.K. Malek, F.R. Ladan, R. Rivoira, T. Moreno, Application of e-beam lithography and reactive ion etching to the fabrication of masks for projection x-ray lithography, Journal of Vacuum Science & Technology B: Microelectronics and Nanometer Structures Processing, Measurement, and Phenomena 9(6) (1991) 3315-3318.
[94] M. Kagias, Z. Wang, P. Villanueva-Perez, K. Jefimovs, M. Stampanoni, 2D-Omnidirectional Hard-X-Ray Scattering Sensitivity in a Single Shot, Physical Review Letters 116(9) (2016) 093902.
[95] A. Pandeshwar, M. Kagias, Z. Shi, M. Stampanoni, Envelope modulated x-ray grating interferometry, Applied Physics Letters 120(19) (2022) 193701.
[96] O.V. Makarova, R. Divan, N. Moldovan, D.A. Czaplewski, M. Esposito, M. Endrizzi, C.-M. Tang, J.D. Ferrara, A. Olivo, Freestanding high-aspect-ratio gold masks for low-energy, phase-based x-ray microscopy, Nanotechnology 34(4) (2023) 045301.

[97] X. Shanshan, L. Jianpeng, Z. Sichao, C. Yifang, Zone shape control by pattern-assisted proximity effect correction in e-beam lithography for efficiency enhancement in x-ray optics, Journal of Micro/Nanolithography, MEMS, and MOEMS 17(4) (2018) 043502.
[98] S. Rutishauser, M. Bednarzik, I. Zanette, T. Weitkamp, M. Börner, J. Mohr, C. David, Fabrication of two-dimensional hard X-ray diffraction gratings, Microelectronic Engineering 101 (2013) 12-16.
[99] J. Chiles, M. Malinowski, A. Rao, S. Novak, K. Richardson, S. Fathpour, Low-loss, submicron chalcogenide integrated photonics with chlorine plasma etching, Applied Physics Letters 106(11) (2015) 111110.
[100] Z. Shi, D. Josell, K. Jefimovs, L. Romano, T.P. Moffat, M. Stampanoni, C.M. Schlepütz, Fabrication of a fractal pattern device for focus characterizations ofX-ray imaging systems by Si deep reactive ion etching and bottom-up Auelectroplating, Appl. Opt. 61(13) (2022) 3850-3854.
[101] J.S. Tobias, K. Frieder, M. Pascal, B. Martin, M. Daniel, K. Danays, E. Sabine, Z. Marcus, B. Tilo, M. Jürgen, Large area gratings by x-ray LIGA dynamic exposure for x-ray phase-contrast imaging, Journal of Micro/Nanolithography, MEMS, and MOEMS 16(1) (2017) 013501.
[102] A. Sarapata, M. Willner, M. Walter, T. Duttenhofer, K. Kaiser, P. Meyer, C. Braun, A. Fingerle, P.B. Noël, F. Pfeiffer, J. Herzen, Quantitative imaging using high-energy X-ray phase-contrast CT with a 70 kVp polychromatic X-ray spectrum, Opt. Express 23(1) (2015) 523-535.
[103] H.H. Solak, C. Dais, F. Clube, Displacement Talbot lithography: a new method for high-resolution patterning of large areas, Opt. Express 19(11) (2011) 10686-10691.
[104] P.-M. Coulon, B. Damilano, B. Alloing, P. Chausse, S. Walde, J. Enslin, R. Armstrong, S. Vézian, S. Hagedorn, T. Wernicke, J. Massies, J. Zúñiga-Pérez, M. Weyers, M. Kneissl, P.A. Shields, Displacement Talbot lithography for nano-engineering of III-nitride materials, Microsystems & Nanoengineering 5(1) (2019) 52.
[105] Z. Shi, K. Jefimovs, M. Stampanoni, L. Romano, High aspect ratio arrays of Si nano-pillars using displacement Talbot lithography and gas-MacEtch, Materials Science in Semiconductor Processing 157 (2023) 107311.
[106] D.L. Voronov, P. Lum, H.A. Padmore, Full size x-ray grating fabrication using large area nanoimprint, Proc.SPIE, 2017, p. 1038607.
[107] D.L. Voronov, S. Park, E.M. Gullikson, F. Salmassi, H.A. Padmore, Advanced low blaze angle x-ray gratings via nanoimprint replication and plasma etch, Opt. Express 31(16) (2023) 26724-26734.
[108] J.A. McCoy, M.A. Verschuuren, D.M. Miles, R.L. McEntaffer, X-ray verification of sol-gel resist shrinkage in substrate-conformal imprint lithography for a replicated blazed reflection grating, OSA Continuum 3(11) (2020) 3141-3156.
[109] J. Sun, Z. Chen, S. Zhou, Y. Sun, Z. Liu, C. Chen, Y. Liu, Y. Sun, M. Wang, S. Xie, W. Liu, Q. Zeng, H. Wu, Z. Bai, Vertical sidewall of silicon nitride mask and smooth surface of etched-silicon simultaneously obtained using CHF3/O2 inductively coupled plasma, Vacuum 207 (2023) 111650.

[110] N.A. Mauchamp, S. Hamaguchi, Molecular dynamics simulation of Si trench etching with SiO2 hard masks, Journal of Vacuum Science & Technology A 40(5) (2022) 053004.
[111] M. Drost, S. Marschmeyer, M. Fraschke, O. Fursenko, F. Bärwolf, I. Costina, M.K. Mahadevaiah, M. Lisker, Etch mechanism of an Al2O3 hard mask in the Bosch process, Micro and Nano Engineering 14 (2022) 100102.
[112] H.S. Alvarez, F.H. Cioldin, A.R. Silva, L.C.J. Espínola, A.R. Vaz, J.A. Diniz, Silicon Micro-Channel Definition via ICP-RIE Plasma Etching Process Using Different Aluminum Hardmasks, Journal of Microelectromechanical Systems 30(4) (2021) 668-674.
[113] R.K. Dey, H. Ekinci, B. Cui, Effects of mask material conductivity on lateral undercut etching in silicon nano-pillar fabrication, Journal of Vacuum Science & Technology B 38(1) (2020) 012207.
[114] J. Kim, M. Kagias, F. Marone, Z. Shi, M. Stampanoni, Fast acquisition protocol for X-ray scattering tensor tomography, Scientific Reports 11(1) (2021) 23046.
[115] B. Wu, A. Kumar, S. Pamarthy, High aspect ratio silicon etch: A review, Journal of Applied Physics 108(5) (2010) 051101.
[116] K. Sato, M. Shikida, Y. Matsushima, T. Yamashiro, K. Asaumi, Y. Iriye, M. Yamamoto, Characterization of orientation-dependent etching properties of single-crystal silicon: effects of KOH concentration, Sensors and Actuators A: Physical 64(1) (1998) 87-93.
[117] X. Chen, S. Jiang, Y. Li, Y. Jiang, W. Wang, Bayanheshig, Fabrication of ultra-high aspect ratio silicon grating using an alignment method based on a scanning beam interference lithography system, Opt. Express 30(22) (2022) 40842-40853.
[118] S. Tan, R. Boudreau, M.L. Reed, Anisotropic Etching of Silicon on${$111$}$ and Near${$111$}$ Planes, Sensors and Materials(Japan) 13(5) (2001) 303-313.
[119] A. Bruccoleri, D. Guan, P. Mukherjee, R.K. Heilmann, M.L. Schattenburg, S. Vargo, Potassium hydroxide polishing of nanoscale deep reactive-ion etched ultrahigh aspect ratio gratings, Journal of Vacuum Science & Technology B 31(6) (2013) 06FF02.
[120] K.H. Ralf, R.B. Alexander, M.G. Eric, G. Hans Moritz, K.S. Randall, L.S. Mark, Improved efficiency critical-angle transmission gratings for high-resolution soft x-ray spectroscopy, Proc.SPIE, 2024, p. 1309313.
[121] S. Surdo, G. Barillaro, Voltage- and Metal-assisted Chemical Etching of Micro and Nano Structures in Silicon: A Comprehensive Review, Small 20(35) (2024) 2400499.
[122] Y. Lei, X. Liu, J. Guo, Z. Zhao, H. Niu, Development of x-ray scintillator functioning also as an analyser grating used in grating-based x-ray differential phase contrast imaging, Chinese Physics B 20(4) (2011) 042901.
[123] X. Li, P.W. Bohn, Metal-assisted chemical etching in HF/H2O2 produces porous silicon, Applied Physics Letters 77(16) (2000) 2572-2574.
[124] H.-D. Um, N. Kim, K. Lee, I. Hwang, J. Hoon Seo, Y.J. Yu, P. Duane, M. Wober, K. Seo, Versatile control of metal-assisted chemical etching for vertical silicon microwire arrays and their photovoltaic applications, Scientific Reports 5(1) (2015) 11277.
[125] Y. Han, J. Jeong, H. Cho, Y. Ahn, S. Park, H. Kim, J.Y. Shin, M.-J. Park, T. Kim, H.-D. Um, Decoding Directional Control in Metal-Assisted Chemical Etching via Catalyst Architecture, Advanced Materials 37(28) (2025) 2502840.

[126] M. Michalska, A. Rossi, G. Kokot, C.M. Macdonald, S. Cipiccia, P.R.T. Munro, A. Olivo, I. Papakonstantinou, Fabrication of High-Aspect Ratio Nanogratings for Phase-Based X-Ray Imaging, Advanced Functional Materials 33(16) (2023) 2212660.
[127] Z. Huang, N. Geyer, P. Werner, J. de Boor, U. Gösele, Metal-Assisted Chemical Etching of Silicon: A Review, Advanced Materials 23(2) (2011) 285-308.
[128] R.P. Srivastava, D.Y. Khang, Structuring of Si into Multiple Scales by Metal-Assisted Chemical Etching, Advanced Materials 33(47) (2021) e2005932.
[129] M.M. Halvorsen, V. Coco, P. Collins, H. Sandaker, L. Romano, Fabrication of a Silicon Electron Multiplier sensor using metal assisted chemical etching and its characterisation, Nuclear Instruments and Methods in Physics Research Section A: Accelerators, Spectrometers, Detectors and Associated Equipment 1060 (2024) 169046.
[130] L. Romano, J. Vila-Comamala, K. Jefimovs, M. Stampanoni, Effect of isopropanol on gold assisted chemical etching of silicon microstructures, Microelectronic Engineering 177 (2017) 59-65.
[131] L. Romano, J. Vila-Comamala, K. Jefimovs, M. Stampanoni, High-Aspect-Ratio Grating Microfabrication by Platinum-Assisted Chemical Etching and Gold Electroplating, Advanced Engineering Materials 22(10) (2020) 2000258.
[132] L. Romano, M. Kagias, K. Jefimovs, M. Stampanoni, Self-assembly nanostructured gold for high aspect ratio silicon microstructures by metal assisted chemical etching, RSC Advances 6(19) (2016) 16025-16029.
[133] F. Marty, L. Rousseau, B. Saadany, B. Mercier, O. Français, Y. Mita, T. Bourouina, Advanced etching of silicon based on deep reactive ion etching for silicon high aspect ratio microstructures and three-dimensional micro- and nanostructures, Microelectronics Journal 36(7) (2005) 673-677.
[134] R. Doering, Y. Nishi, Handbook of Semiconductor Manufacturing Technology, Second ed., CRC Press.2008.
[135] K. Nojiri, Mechanism of Dry Etching, in: K. Nojiri (Ed.), Dry Etching Technology for Semiconductors, Springer International Publishing, Cham, 2015, pp. 11-30.
[136] R. Barnett, D. Thomas, Y. Song, D. Tossell, T. Barrass, O. Ansell, A new plasma source for next generation MEMS deep Si etching: Minimal tilt, improved profile uniformity and higher etch rates, 2010 Proceedings 60th Electronic Components and Technology Conference (ECTC), 2010, pp. 1056-1059.
[137] F. Laermer, S. Franssila, L. Sainiemi, K. Kolari, Chapter 16 - Deep reactive ion etching, in: M. Tilli, M. Paulasto-Krockel, M. Petzold, H. Theuss, T. Motooka, V. Lindroos (Eds.), Handbook of Silicon Based MEMS Materials and Technologies (Third Edition), Elsevier2020, pp. 417-446.
[138] F. Laerme, A. Schilp, K. Funk, M. Offenberg, Bosch deep silicon etching: improving uniformity and etch rate for advanced MEMS applications, Technical Digest. IEEE International MEMS 99 Conference. Twelfth IEEE International Conference on Micro Electro Mechanical Systems (Cat. No.99CH36291), 1999, pp. 211-216.
[139] P. Moroz, D.J. Moroz, Numerical Simulation of Bosch Processing for Deep Silicon Plasma Etching, Journal of Physics: Conference Series 550(1) (2014) 012030.

[140] G. Feng, Y. Sami, K. Markku, K. Markku, Smooth silicon sidewall etching for waveguide structures using a modified Bosch process, Journal of Micro/Nanolithography, MEMS, and MOEMS 13(1) (2014) 1-6.
[141] V. Revol, X-ray phase contrast imaging by grating interferometry, Zürich, 2011.
[142] G. Kokkoris, V. Constantoudis, P. Angelikopoulos, G. Boulousis, E. Gogolides, Dual nanoscale roughness on plasma-etched Si surfaces: Role of etch inhibitors, Physical Review B 76(19) (2007) 193405.
[143] A. Bagolini, P. Scauso, S. Sanguinetti, P. Bellutti, Silicon Deep Reactive Ion Etching with aluminum hard mask, Materials Research Express 6(8) (2019) 085913.
[144] B. Mimoun, H.T.M. Pham, V. Henneken, R. Dekker, Residue-free plasma etching of polyimide coatings for small pitch vias with improved step coverage, Journal of Vacuum Science & Technology B 31(2) (2013) 021201.
[145] D. Sameoto, Y.S. Li, C. Menon, Micromask Generation for Polymer Morphology Control: Nanohair Fabrication for Synthetic Dry Adhesives, Advances in Science and Technology 54 (2009) 439-444.
[146] C.M. Silvestre, V. Nguyen, H. Jansen, O. Hansen, Deep reactive ion etching of 'grass-free' widely-spaced periodic 2D arrays, using sacrificial structures, Microelectronic Engineering 223 (2020) 111228.
[147] Z. Fan, D. Cui, Z. Zhang, Z. Zhao, H. Chen, Y. Fan, P. Li, Z. Zhang, C. Xue, S. Yan, Recent Progress of Black Silicon: From Fabrications to Applications, Nanomaterials, 2021.
[148] D. Schmelz, T. Käsebier, Z. Shi, Q. Cheng, N. Sergeev, D. Schelle, U. Zeitner, Investigations on black silicon nanostructures fabricated by reactive ion etching on highly curved surfaces, Materials Science in Semiconductor Processing 165 (2023) 107646.
[149] D. Pradeep, M. Jianmin, Effect of SF6 flow rate on the etched surface profile and bottom grass formation in deep reactive ion etching process, Journal of Physics: Conference Series 34(1) (2006) 577.
[150] Y. Lin, R. Yuan, C. Zhou, Z. Dong, Z. Su, H. Zhang, Z. Chen, Y. Li, C. Wang, The application of the scallop nanostructure in deep silicon etching, Nanotechnology 31(31) (2020) 315301.
[151] L. Filipovic, S. Selberherr, The effects of etching and deposition on the performance and stress evolution of open through silicon vias, Microelectronics Reliability 54(9) (2014) 1953-1958.
[152] Z. Cheng, Y. Ding, L. Xiao, X. Wang, Z. Chen, Comparative evaluations on scallop-induced electric-thermo-mechanical reliability of through-silicon-vias, Microelectronics Reliability 103 (2019) 113512.
[153] A.M. Baracu, C.A. Dirdal, A.M. Avram, A. Dinescu, R. Muller, G.U. Jensen, P.C. Thrane, H. Angelskår, Metasurface Fabrication by Cryogenic and Bosch Deep Reactive Ion Etching, Micromachines, 2021.
[154] Y. Lin, R. Yuan, X. Zhang, Z. Chen, H. Zhang, Z. Su, S. Guo, X. Wang, C. Wang, Deep Dry Etching of Silicon with Scallop Size Uniformly Larger than 300 nm, Silicon 11(2) (2019) 651-658.

[155] J.S. Park, D.-H. Kang, S.M. Kwak, T.S. Kim, J.H. Park, T.G. Kim, S.-H. Baek, B.C. Lee, Low-temperature smoothing method of scalloped DRIE trench by post-dry etching process based on SF6 plasma, Micro and Nano Systems Letters 8(1) (2020) 14.
[156] N. Roxhed, P. Griss, G. Stemme, A method for tapered deep reactive ion etching using a modified Bosch process, Journal of Micromechanics and Microengineering 17(5) (2007) 1087.
[157] B. Chang, P. Leussink, F. Jensen, J. Hübner, H. Jansen, DREM: Infinite etch selectivity and optimized scallop size distribution with conventional photoresists in an adapted multiplexed Bosch DRIE process, Microelectronic Engineering 191 (2018) 77-83.
[158] H. Miao, L. Chen, M. Mirzaeimoghri, R. Kasica, H. Wen, Cryogenic Etching of High Aspect Ratio 400-nm Pitch Silicon Gratings, Journal of Microelectromechanical Systems 25(5) (2016) 963-967.
[159] V.T.H. Nguyen, E. Shkondin, F. Jensen, J. Hübner, P. Leussink, H. Jansen, Ultrahigh aspect ratio etching of silicon in SF6-O2 plasma: The clear-oxidize-remove-etch (CORE) sequence and chromium mask, Journal of Vacuum Science & Technology A 38(5) (2020) 053002.
[160] W. Zhang, R. Huang, Q. Gao, Etching of smoothing/without undercutting deep trench in silicon with SF6/O2 containing plasmas, Engineering Research Express 3(3) (2021) 035048.
[161] M. Boufnichel, P. Lefaucheux, S. Aachboun, R. Dussart, P. Ranson, Origin, control and elimination of undercut in silicon deep plasma etching in the cryogenic process, Microelectronic Engineering 77(3) (2005) 327-336.
[162] Y. Zhang, Z. Hou, C. Si, G. Han, Y. Zhao, X. Lu, J. Liu, J. Ning, F. Yang, Effects of Mask Material on Lateral Undercut of Silicon Dry Etching, Micromachines, 2023.
[163] R. Knizikevičius, V. Kopustinskas, Influence of temperature on the etching rate of SiO2 in CF4+O2 plasma, Microelectronic Engineering 83(2) (2006) 193-196.
[164] S. Tachi, K. Tsujimoto, S. Arai, T. Kure, Low-temperature dry etching, Journal of Vacuum Science & Technology A 9(3) (1991) 796-803.
[165] L. Hsu, W. Lai, J. Kim, E. Cheng, P. Lin, Eliminating undercut profile of through silicon via by using nitrided fluorocarbon passivation in rapid alternating process, 2016 e-Manufacturing and Design Collaboration Symposium (eMDC), 2016, pp. 1-3.
[166] A. Momose, Z. Zhao, R. Ueda, M. Cai, H. Takano, Y. Wu, K. Ikematsu, H. Kawakami, P. Zangi, P. Meyer, M. Börner, J. Schulz, Development of grating-based super-resolution x-ray phase imaging, AIP Conference Proceedings 2990(1) (2023).
[167] A. Yaroshenko, M. Bech, G. Potdevin, A. Malecki, T. Biernath, J. Wolf, A. Tapfer, M. Schüttler, J. Meiser, D. Kunka, M. Amberger, J. Mohr, F. Pfeiffer, Non-binary phase gratings for x-ray imaging with a compact Talbot interferometer, Opt. Express 22(1) (2014) 547-556.
[168] T. Xu, Z. Tao, H. Li, X. Tan, H. Li, Effects of deep reactive ion etching parameters on etching rate and surface morphology in extremely deep silicon etch process with high aspect ratio, Advances in Mechanical Engineering 9(12) (2017) 1687814017738152.
[169] W. Yashiro, Y. Takeda, A. Momose, Efficiency of capturing a phase image using cone-beam x-ray Talbot interferometry, J. Opt. Soc. Am. A 25(8) (2008) 2025-2039.

[170] T. Kim, J. Lee, Optimization of deep reactive ion etching for microscale silicon hole arrays with high aspect ratio, Micro and Nano Systems Letters 10(1) (2022) 12.
[171] L. Feng, S. Zeng, Y. Su, L. Wang, Y. Xu, S. Guo, S. Chen, Y. Ji, X. Peng, Z. Wu, S. Wang, Process Optimization and Performance Evaluation of TSV Arrays for High Voltage Application, Micromachines, 2023.
[172] M.A. Gosalvez, Y. Zhou, Y. Zhang, G. Zhang, Y. Li, Y. Xing, Simulation of microloading and ARDE in DRIE, 2015 Transducers - 2015 18th International Conference on Solid-State Sensors, Actuators and Microsystems (TRANSDUCERS), 2015, pp. 1255-1258.
[173] M.S. Gerlt, N.F. Läubli, M. Manser, B.J. Nelson, J. Dual, Reduced Etch Lag and High Aspect Ratios by Deep Reactive Ion Etching (DRIE), Micromachines, 2021.
[174] X. Wang, Q. Wang, J. Zhou, Inverse RIE micro-loading in deep etching of silicon via array, 2019 IEEE 13th International Conference on ASIC (ASICON), 2019, pp. 1-3.
[175] J.-K. Lee, I.-Y. Jang, S.-H. Lee, C.-K. Kim, S.H. Moon, Mechanism of Sidewall Necking and Bowing in the Plasma Etching of High Aspect-Ratio Contact Holes, Journal of The Electrochemical Society 157(3) (2010) D142.
[176] M. Wang, M.J. Kushner, High energy electron fluxes in dc-augmented capacitively coupled plasmas. II. Effects on twisting in high aspect ratio etching of dielectrics, Journal of Applied Physics 107(2) (2010) 023309.
[177] S. Huang, S. Shim, S.K. Nam, M.J. Kushner, Pattern dependent profile distortion during plasma etching of high aspect ratio features in SiO2, Journal of Vacuum Science & Technology A 38(2) (2020) 023001.
[178] M.Y. Yoon, H.J. Yeom, J.H. Kim, J.-R. Jeong, H.-C. Lee, Plasma etching of the trench pattern with high aspect ratio mask under ion tilting, Applied Surface Science 595 (2022) 153462.
[179] Z. Shi, K. Jefimovs, A. La Magna, M. Stampanoni, L. Romano, High aspect ratio tilted gratings through local electric field modulation in plasma etching, Applied Surface Science 588 (2022) 152938.
[180] Z. Shi, K. Jefimovs, L. Romano, J. Vila-Comamala, M. Stampanoni, Laboratory X-ray interferometry imaging with a fan-shaped source grating, Opt. Lett. 46(15) (2021) 3693-3696.
[181] J. Song, R.K. Heilmann, A.R. Bruccoleri, M.L. Schattenburg, Characterizing profile tilt of nanoscale deep-etched gratings via x-ray diffraction, Journal of Vacuum Science & Technology B 37(6) (2019) 062917.
[182] K.H. Ralf, R.B. Alexander, M.G. Eric, K.S. Randall, L.S. Mark, Soft x-ray performance and fabrication of flight-like blazed transmission gratings for the x-ray spectrometer on Arcus probe, Proc.SPIE, 2023, p. 126790L.
[183] W. Cui, X. Li, S. Zhou, J. Weng, Investigation on process parameters of electrospinning system through orthogonal experimental design, Journal of Applied Polymer Science 103(5) (2007) 3105-3112.
[184] S.K. Karna, R. Sahai, Others, An overview on Taguchi method, International journal of engineering and mathematical sciences 1(1) (2012) 1-7.

[185] B.L. Henke, E.M. Gullikson, J.C. Davis, X-Ray Interactions: Photoabsorption, Scattering, Transmission, and Reflection at E = 50-30,000 eV, Z = 1-92, Atomic Data and Nuclear Data Tables 54(2) (1993) 181-342.
[186] B. Rösner, F. Koch, F. Döring, J. Bosgra, V.A. Guzenko, E. Kirk, M. Meyer, J.L. Ornelas, R.H. Fink, S. Stanescu, S. Swaraj, R. Belkhou, B. Watts, J. Raabe, C. David, Exploiting atomic layer deposition for fabricating sub-10nm X-ray lenses, Microelectronic Engineering 191 (2018) 91-96.
[187] C. Chang, A. Sakdinawat, Ultra-high aspect ratio high-resolution nanofabrication for hard X-ray diffractive optics, Nature Communications 5(1) (2014) 4243.
[188] R. Akan, T. Frisk, F. Lundberg, H. Ohlin, U. Johansson, K. Li, A. Sakdinawat, U. Vogt, Metal-Assisted Chemical Etching and Electroless Deposition for Fabrication of Hard X-ray Pd/Si Zone Plates, Micromachines 11(3) (2020) 301.
[189] Y. Lei, Q. Li, F. Wali, X. Liu, G. Xu, J. Li, J. Huang, Tungsten nanoparticles-based x-ray absorption gratings for cascaded Talbot–Lau interferometers, Journal of Micromechanics and Microengineering 29(11) (2019) 115008.
[190] Y. Lei, G. Xu, F. Wali, Q. Li, X. Liu, J. Huang, J. Li, An 8-inch absorption grating used in cascaded Talbot-Lau interferometers for X-ray phase-contrast imaging, Applied Physics Express 12(12) (2019) 126504.
[191] C. Arboleda, Z. Wang, T. Koehler, G. Martens, U. Van Stevendaal, M. Bartels, P. Villanueva-Perez, E. Roessl, M. Stampanoni, Sensitivity-based optimization for the design of a grating interferometer for clinical X-ray phase contrast mammography, Opt. Express 25(6) (2017) 6349-6364.
[192] A.P. Sauter, J. Andrejewski, F. De Marco, K. Willer, L.B. Gromann, W. Noichl, F. Kriner, F. Fischer, C. Braun, T. Koehler, F. Meurer, A.A. Fingerle, D. Pfeiffer, E. Rummeny, J. Herzen, F. Pfeiffer, Optimization of tube voltage in X-ray dark-field chest radiography, Scientific Reports 9(1) (2019) 8699.
[193] Y. Lei, Y. Du, J. Li, J. Huang, Z. Zhao, X. Liu, J. Guo, H. Niu, Application of Bi Absorption Gratings in Grating-Based X-ray Phase Contrast Imaging, Applied Physics Express 6(11) (2013) 117301.
[194] L. Romano, J. Vila-Comamala, H. Schift, M. Stampanoni, K. Jefimovs, Hot embossing of Au- and Pb-based alloys for x-ray grating fabrication, Journal of Vacuum Science & Technology B 35(6) (2017) 06G302.
[195] S. Ambrozik, T.P. Moffat, C. Zhang, H. Miao, D. Josell, Bottom-Up Gold Filling of High Aspect Ratio Trenches, Journal of The Electrochemical Society 166(10) (2019) D443-D451.
[196] L. Romano, M. Stampanoni, Microfabrication of X-ray Optics by Metal Assisted Chemical Etching: A Review, Micromachines (Basel) 11(6) (2020) 589.
[197] S. Spindler, D. Etter, M. Rawlik, M. Polikarpov, L. Romano, Z. Shi, K. Jefimovs, Z. Wang, M. Stampanoni, The choice of an autocorrelation length in dark-field lung imaging, Scientific Reports 13(1) (2023) 2731.
[198] J. Baborowski, V. Revol, C. Kottler, R. Kaufmann, P. Niedermann, F. Cardot, A. Dommann, A. Neels, M. Despont, High aspect ratio, Large area silicon-based gratings for X-ray phase contrast imaging, 2014 IEEE 27th International Conference on Micro Electro Mechanical Systems (MEMS), 2014, pp. 490-493.

[199] S.A. Znati, N. Chedid, H. Miao, L. Chen, E.E. Bennett, H. Wen, Electrodeposition of Gold to Conformally Fill High Aspect Ratio Nanometric Silicon Grating Trenches: A Comparison of Pulsed and Direct Current Protocols, Journal of surface engineered materials and advanced technology 5(4) (2015) 207.
[200] K. Jefimovs, J. Vila-Comamala, T. Pilvi, J. Raabe, M. Ritala, C. David, Zone-Doubling Technique to Produce Ultrahigh-Resolution X-Ray Optics, Physical Review Letters 99(26) (2007) 264801.
[201] R.P. Seisyan, Nanolithography in microelectronics: A review, Technical Physics 56(8) (2011) 1061-1073.
[202] T.P. Moffat, D. Wheeler, M.D. Edelstein, D. Josell, Superconformal film growth: Mechanism and quantification, IBM Journal of Research and Development 49(1) (2005) 19-36.
[203] T.P. Moffat, D. Josell, Extreme Bottom-Up Superfilling of Through-Silicon-Vias by Damascene Processing: Suppressor Disruption, Positive Feedback and Turing Patterns, Journal of The Electrochemical Society 159(4) (2012) D208.
[204] T.P. Moffat, T.M. Braun, D. Raciti, D. Josell, Superconformal Film Growth: From Smoothing Surfaces to Interconnect Technology, Accounts of Chemical Research 56(9) (2023) 1004-1017.
[205] D. Josell, T.M. Braun, T.P. Moffat, Mechanism of Bismuth Stimulated Bottom-up Gold Feature Filling, Journal of The Electrochemical Society 169(12) (2022) 122507.
[206] D. Josell, T.P. Moffat, Extreme Bottom-up Gold Filling of High Aspect Ratio Features, Accounts of Chemical Research 56(6) (2023) 677-688.
[207] D. Josell, D. Raciti, T. Gnaupel-Herold, A. Pereira, V. Tsai, Q. Yu, L. Chen, M. Stauber, M. Rawlik, M. Stampanoni, T.P. Moffat, L. Romano, Bottom-up Gold Filling of Trenches in Curved Wafers, Journal of The Electrochemical Society 171(3) (2024) 032502.
[208] D. Josell, W.A. Osborn, M.E. Williams, H. Miao, Robust Bottom-Up Gold Filling of Deep Trenches and Gratings, Journal of The Electrochemical Society 169(3) (2022) 032509.
[209] A. Rossi, I. Buchanan, A. Astolfo, M. Michalska, D. Briglin, A. Charman, D. Josell, A. Olivo, I. Papakonstantinou, Fabrication of Ultra-Thick Masks for X-Ray Phase Contrast Imaging at Higher Energy, Advanced Materials Interfaces 12(8) (2025) 2400749.
[210] D. Josell, K. Jefimovs, L. Romano, Bottom-up Gold Filling of Sub-Micrometer Trenches, Journal of The Electrochemical Society 172(4) (2025) 042502.
[211] L. Romano, Etching: The Art of Semiconductor Micromachining, Micromachines 16(2) (2025) 213.
[212] M. Rawlik, A. Pereira, S. Spindler, Z. Wang, L. Romano, K. Jefimovs, Z. Shi, M. Polikarpov, J. Xu, M.-C. Zdora, S. van Gogh, M. Stauber, E.G. Yukihara, J.B. Christensen, R.A. Kubik-Huch, T. Niemann, C. Leo, Z. Varga, A. Boss, M. Stampanoni, Increased dose efficiency of breast CT with grating interferometry, Optica 10(7) (2023) 938-943.
[213] Z. Rongchun, Z. Haixia, H. Yilong, W. Yangyuan, Simulation of the Bosch process with a string–cell hybrid method, Journal of Micromechanics and Microengineering 14(7) (2004) 851.

[214] G. Le Dain, A. Rhallabi, M.C. Fernandez, M. Boufnichel, F. Roqueta, Multiscale approach for simulation of silicon etching using SF6/C4F8 Bosch process, Journal of Vacuum Science & Technology A 35(3) (2017) 03E113.
[215] T. Dobashi, H. Kobayashi, Y. Okuyama, T. Ohmori, Effect of initial-learning dataset on etching profile optimization using machine learning in plasma etching, Japanese Journal of Applied Physics 62(SI) (2023) SI1016.
[216] K. Kara, M. Leandro, T.B. Roger, J.C. Meghali, Automated, high throughput optimization of multistep and cyclic etch and deposition processes using SandBox Studio AI, Proc.SPIE, 2022, p. 1205608.
[217] A.P. Milenin, B.T. Chan, F. Lazzarino, Assessment of STI dry etch process variability by means of dynamic time warping technique, Japanese Journal of Applied Physics 62(SI) (2023) SI1004.
[218] G. Deepak, N. Sravan, M. Takemasa, J. Oliver, B. Waheb, C. Steven, L. Kyeong-tae, K. Andre, K. Sangdoo, U. Youngje, K. Ki-il, P. Changbae, S. Myeonggil, B. Keun Hee, AppliedPRO: process recipe optimizer for R&D acceleration and beyond, Proc.SPIE, 2023, p. 1249903.
[219] L. Zhao, Y. Zhu, T. Zhao, Deep Learning-Based Remaining Useful Life Prediction Method with Transformer Module and Random Forest, Mathematics, 2022.
[220] D. Noda, M. Tanaka, K. Shimada, T. Hattori, Fabrication of Diffraction Grating with High Aspect Ratio Using X-ray Lithography Technique for X-ray Phase Imaging, Japanese Journal of Applied Physics 46(2R) (2007) 849.